This is a preprint, the final version is subject to change, of the American Mineralogist (MSA)
Cite as Authors (Year) Title. American Mineralogist, in press.
DOI: https://doi.org/10.2138/am-2020-7159

Revision 1

Changes of antigorite cell parameters close to the antigorite dehydration reaction at subduction zone conditions

TINGTING SHEN[1], CONG ZHANG[1,5*], JING CHEN[2], JÖRG HERMANN[3,6], LIFEI ZHANG[4], JOSÉ ALBERTO PADRÓN-NAVARTA[7], LI CHEN[2], JUN XU[2], JINGSUI YANG[1]

[1] Key Laboratory of Deep-Earth Dynamics of Ministry of Natural Resources, Institute of Geology, Chinese Academy of Geological Sciences, Beijing 100037, China

[2] Electron Microscopy Laboratory, Peking University, Beijing 100871, China

[3] Research School of Earth Sciences, the Australian National University, Canberra ACT 0200, Australia

[4]Department of Geology, School of Earth and Space Sciences, Peking University, Beijing 100871, China

[5] College of Earth Science and Engineering, Shandong University of Science and Technology, Qingdao 266510, China

[6] Institute of Geological Sciences, University of Bern 3012, Switzerland

[7] Géosciences Montpellier, CNRS & Université de Montpellier, F-34095 Montpellier Cedex 5, France

* Corresponding author email: congzhang@pku.edu.cn

ABSTRACT

The length of the antigorite *a*-axis (usually expressed as the polysome *m* value) has been investigated as a function of temperature and pressure in the range of 600-650 °C, 25-45 kbar in weeklong piston cylinder experiments. A well-characterised natural antigorite (with *m*=16 and less abundant *m*=15) was used as starting material that coexisted with olivine, chlorite, Ti-humite phases and aqueous

fluid at run conditions. Transmission electron microscope (TEM) measurements on selected FIB wafers showed that antigorite *m* values after the experiments varied between 14 and 22. More than 40 punctual analyses for each run condition were acquired to determine the range and the dominant *m* value. The antigorite peak *m* value decreased systematically from 17-19 at 600 °C to 15-16 at 650°C. The spacing of the *m*-isolines is getting narrower as the antigorite breakdown reaction is approached. The topology of the *m*-isolines is similar to previous experiments in the simple MSH-system, however the isolines are shifted to about 50-100°C higher temperatures due to the incorporation of Al into antigorite. Powder samples and FIB wafers of natural antigorite from the Tianshan UHP belt (China) with peak metamorphic conditions of ~35 kbar, ~520 °C were also investigated with TEM. Low Al-antigorite formed at peak metamorphic conditions displays a peak *m* value of 20-21, whereas high-Al antigorite formed during isothermal decompression displays a lower *m* value of 19. The experimental results and the new UHP antigorite measurements are combined with published data of *m* values from metamorphic antigorite that experienced variable conditions in order to construct a P-T-*m* diagram that can be used in future studies to better constrain formation conditions of serpentinites. The decrease of *m* values and the increase of Al in antigorite with increasing temperature result in a small, continuous dehydration whereby the H_2O content of antigorite changes from 12.4 to 12.1 wt.%. Therefore, it is expected that a pore fluid is present during the prograde deformation of serpentinites. TEM observations on the experiments showed that antigorite adjusted its Al content by segregation of chlorite at the nanoscale. Together with the observation that always multiple *m* values are present in a single sample this indicates that full equilibration of antigorite at the micron-scale is rare, with important implications for the interpretation of geochemical signatures obtained by *in-situ* techniques.

Keywords: Antigorite, polysomatism, TEM, high-pressure experiments, serpentinite

This is a preprint, the final version is subject to change, of the American Mineralogist (MSA)
Cite as Authors (Year) Title. American Mineralogist, in press.
DOI: https://doi.org/10.2138/am-2020-7159

INTRODUCTION

Antigorite is a high temperature and pressure serpentine variety (Evans et al. 1976), and the most abundant hydrous phase in subducted ultramafic rocks down to approximately 100 km depth (e.g. Ulmer and Trommsdorff 1995, 1999; Wunder and Schreyer 1997; Schmidt and Poli 1998; Wunder et al. 2001; Scambelluri et al. 2001, 2004a, 2004b; Bromiley and Pawley 2003; Hattori and Guillot 2003, 2007; Shen et al. 2015; Maurice et al. 2018). Serpentinites usually form by reaction of mantle rocks with seawater-derived fluids during ocean floor alteration (e.g. Bonatti and Crane 1984). Additionally, parts of the mantle wedge might also become serpentinized above the subduction channel when fluids are released during prograde metamorphism of sediments and mafic crust (e.g. Iwamori and Zhao 2000; Kawakatsu and Watada 2007). Lizardite- and chrysotile-rich serpentinites are characteristic of low-temperature and low-pressure metamorphic conditions (e.g. Janecky and Seyfried 1986; Evans 2004, 2013; Schwartz et al. 2013; Ghaderi et al. 2015). Antigorite then forms from lizardite or chrysotile (with an ideal structural formula $Mg_3Si_2O_5(OH)_4$) with increasing pressure and temperature at lower greenschist facies conditions (e.g. Trommsdorff and Evans 1974; Frost 1975; Evans et al. 1976; Mellini et al. 1987; Worden et al. 1991). Antigorite contains ~12.5 wt.% water in the crystal structure and thus antigorite-serpentinites can carry large amounts of water into the mantle (e.g. Ulmer and Trommsdorff 1995; Wunder and Schreyer 1997; Trommsdorff et al. 1998; Wunder et al. 2001; Scambelluri et al. 2001, 2004a, b; Hattori and Guillot 2003, 2007; Deschamps et al. 2010, 2013; Padrón-Navarta et al. 2011, 2013, 2015). Experimental and natural studies provide evidence that antigorite breakdown occurs at sub-arc depth and the liberated fluids contribute to partial melting of the mantle wedge, deep earthquakes and influence global water recycling (Fig. 1; Ulmer and Trommsdorff 1995; Scambelluri et al. 1995; Wunder and Schreyer 1997; Bromiley and Pawley 2003; Garrido et al. 2005; Reynard and Wunder 2006; Padrón-Navarta and Hermann 2017; Maurice et al. 2018). Studies on natural

high-pressure serpentinites have also highlighted their importance for coupled water and trace element recycling (e.g. Garrido et al. 2005; Bebout et al. 2007; Deschamps et al. 2012, 2013; Debret et al. 2013; Marchesi et al. 2013; Harvey et al. 2014; Bretscher et al. 2018; Scambelluri et al. 2019).

Lizardite and chrysotile display a flat layer structure (e.g. Jahanbagloo and Zoltai 1968) or cylindrical/spiral tubes (e.g. Whittaker 1953, 1956), respectively. Antigorite is characterized by a modulated wave-like structure with changes in the layer polarity to compensate small misfits between the tetrahedral and octahedral layers (e.g. Zussman 1954; Kunze 1956, 1958; Mellini et al. 1987; Capitani and Mellini 2004). The wavelength is variable and is expressed in terms of the number of tetrahedra (*m*) occurring along an entire wave (Uehara 1998; Wunder et al. 2001; Mellini et al. 1987). Kunze (1961) generalized the composition of individual antigorite by the formula $M_{3m-3}T_{2m}O_{5m}(OH)_{4m-6}$ (*m* is the number of tetrahedra in a single chain defined by the wavelength *a*, M=octahedral cations (Mg, Fe^{2+}, Fe^{3+}, Cr^{3+}, Ni, Mn^{2+}, Al); T= tetrahedral cations (Si, Al)). Antigorite forms a polysomatic series of compositions and varies by changing the *m* value (Thompson 1978). The compositions are chemographically collinear with chrysotile/lizardite ($m=\infty$) and talc ($m=2$), as a series of discrete points (Mellini et al. 1987). The basic unit cell of ideal antigorite ($m=17$) is monoclinic P*m* space group with $a=43.3$ Å, $b=9.2$ Å, $c=7.3$ Å, $\beta=91.4$ (Aruja 1944; Mellini et al. 1987) or $a=43.505(6)$ Å, $b=9.251(1)$ Å, $c=7.263(1)$ Å, $\beta=91.32(1)$ (Capitani and Mellini 2004), or *C*2/*m* in the $m=16$ polysome, with lattice parameters of $a=81.664(10)$ Å, $b=9.255(5)$ Å, $c=7.261(5)$ Å, $\beta=91.409(5)$ (Capitani and Mellini 2006). As suggested by Mellini et al. (1987), the *m* values of antigorite commonly range from 23 to 14 in natural metamorphic serpentinites. Transmission electron microscopy (TEM) studies and thermodynamic calculations both indicate that antigorite with high *m* values are more stable at low temperature, while those with low *m* values are more stable at high temperature (Kunze 1961; Trommsdorff 1983; Uehara and Kamata 1994; Mellini et al. 1987). Wunder et al. (2001) performed an experimental study ranging from 350-710 °C, 2-50 kbar in the simple MSH system and found that the *a*-axis (related to the *m* value) is roughly negatively correlated with

113 temperature but positively correlated with pressure. Most studies observed quite a
114 large range of *m* values within a single sample and even at the grain scale (e.g. Mellini
115 et al. 1987; Wunder et al. 2001) and thus were cautious in using the *m* value as
116 potential geothermobarometer. Nevertheless, several studies on natural samples
117 showed that the structure of antigorite in metamorphosed serpentinites systematically
118 changes with changing pressure and temperature (e.g. Mellini et al. 1987; Viti and
119 Mellini 1996; Auzende et al. 2002, 2006; Padrón-Navarta et al. 2008). This is a
120 significant finding as antigorite has a large stability field and therefore it is
121 challenging to obtain information on the formation conditions of antigorite in
122 subducted rocks. One way to obtain constraints on metamorphic conditions comes
123 from the Tschermak exchange in antigorite in chlorite-buffered assemblages
124 (Padrón-Navarta et al. 2013). The systematic change in *m* values would provide an
125 additional avenue to further constrain the metamorphic conditions of subducted
126 serpentinites but so far, no experimental data for natural compositions are available.
127 In this study, we performed TEM measurements on antigorite produced in piston
128 cylinder, high-pressure experiments in order to track changes in the antigorite
129 structure at different temperatures and pressures. We used a well-equilibrated natural
130 antigorite containing also Al, Fe and Cr with a well-defined *m* value. Experiments
131 were conducted close to the antigorite breakdown reaction at conditions relevant for
132 subduction zone metamorphism. The experimental results are compared with data
133 from natural samples to evaluate to what extent the cell parameters of antigorite can
134 be used as a P-T indicator for subducted serpentinites. The combined influence of
135 changing antigorite composition and structure on fluid liberation during ongoing
136 subduction will also be discussed.
137 Mineral abbreviations used in the text, figures and tables all follow Whitney and
138 Evans (2010): Atg=antigorite, Brc=brucite, Chl=chlorite, Chr=chromite,
139 Cr-Spl=Cr-spinel, En=enstatite, Grt=garnet, Ilm=ilmenite, Liz=lizardite; Ol=olivine,
140 Opx=orthopyroxene, PhA=phase A, Rt=rutile, Tlc=talc. And TiCh=Ti-chondrodite,
141 TiCl=Ti-clinohumite.

This is a preprint, the final version is subject to change, of the American Mineralogist (MSA)
Cite as Authors (Year) Title. American Mineralogist, in press.
DOI: https://doi.org/10.2138/am-2020-7159

METHODS, SAMPLES AND SAMPLE PREPARATION

Material characterization and experimental approach

The antigorite samples used in this study were equilibrated in piston cylinder experiments at the Research School of Earth Sciences (RSES), Australian National University. The experiments were initially designed to determine the stability fields of Ti-chondrodite and Ti-clinohumite in natural serpentinites (Shen et al. 2015). The starting material consists of 73 wt.% antigorite (sample Al06-44, Cerro del Almirez, Spain, Padrón-Navarta et al. 2008, 2011, 2012, 2013; Debret et al. 2015; Scicchitano et al. 2018), 9.8 wt.% Ti-clinohumite (Malenco, Italy), 9 wt.% brucite (synthetic), 3 wt.% Ti-chondrodite (Tianshan, China, Shen et al. 2014), 3 wt.% olivine (Fo_{90}, San Carlos) and 2.2 wt.% ilmenite (Duria peridotites, Alps, Hermann et al. 2006). The mineral blend was well mixed and ground in a mortar to less than 200 mesh grid. The mixture (20 mg) with no additional water was loaded into a 2.3 mm outer diameter Au capsule and then sealed by arc welding. The gold capsule was set in MgO surrounded by a graphite heater and placed in a low friction Teflon foil-salt assembly. Experiments were run in 150 and 200 tonne presses. Refer to Shen et al. (2015) for a detailed description of the experimental technique. After the experiments, the capsules were sectioned in half, embedded in epoxy and polished with diamond pastes. Among all the experiments, 5 run products were chosen to study the antigorite cell parameters, which are D1512, C4408, D1526, C4429 and C4442 (Table 1). The P-T ranges between 600-650 °C and 25-45 kbar, close to the maximum stability of antigorite.

The natural antigorite investigated in detail in this study is from South-Western Tianshan, China (sample C11107). This serpentinized Ti-chondrodite bearing wehrlite sample experienced peak metamorphic conditions of 510-530 °C, 37±7 kbar (Shen et al. 2015). The peak metamorphic mineral assemblage comprises Ti-chondrodite+olivine+antigorite+chlorite+magnetite+brucite. Two generations of antigorite can be identified based on its aluminium content. Low aluminium (low-Al, such as 1.11 wt.%) antigorite was formed at peak ultrahigh pressure (UHP)

metamorphic conditions whereas high aluminium (high-Al, such as 3.38 wt.%) antigorite was formed at lower pressure (10-20 kbar) and slightly lower temperatures of ~500 °C (Shen et al. 2015). The low-Al antigorite investigated by TEM (see below) was included in Ti-chondrodite whereas the high-Al antigorite is from the matrix.

Backscattered electron (BSE) images were taken on a FEI Strata DB 235 scanning electron microscope (SEM) in the Electron Microscopy Laboratory, Peking University, China (Chen et al. 2015).

Mineral compositions from the experimental runs were determined using a JEOL JSM6400 scanning electron microscope (SEM) at the Australian National University with an Oxford Instruments Pentafet LINK ISIS energy-dispersive spectrometry (EDS) system. Operating conditions were a 15 kV accelerating voltage, 1 nA beam current and 100 s acquisition time. Sanidine (Si and K), MgO (Mg), diopside (Ca), albite (Na and Al), rutile (Ti), synthetic spessartine (Mn), Cr_2O_3 (Cr), Fe_2O_3 (Fe) and pure Ni served as standards. Results were quantified with the ZAF algorithm implemented in the Oxford SEMQuant software. Detection limits for these conditions are between 0.15-0.20 wt.%. The compositions of antigorite in the starting material and from different runs are presented in Table 2. The compositions of antigorite in the natural sample investigated by FIB-TEM (Table 3) were obtained with a JXA-8800R electron microprobe at Peking University operated at 15 kV acceleration voltage and 20 nA beam current. The beam diameter is 2 μm and the counting time on peak for each element was 10-15 s. Natural jadeite (Si), forsterite (Mg), hematite (Fe), albite (Na, Al), rutile (Ti), rhodonite (Mn) and sanidine (K) served as standards.

Raman spectra were collected at the Raman Lab in the Institute of Geology, Chinese Academy of Geological Sciences (Beijing, China) with a Horiba spectrometer LabRAM HR evolution equipped with an Olympus BX41 light microscope and calibrated by a silicon wafer with 520.7 cm^{-1} Raman shift. Raman spectra were excited by a 532 nm Nd: YAG laser with 100 mW laser power and received by a 600 g optical grating through an 80 μm confocal hole. The resolution is about 1-1.5 cm^{-1}. The data was processed by the LabSpec 6 software.

Transmission Electron Microscopy

For each experimental run product, two to three antigorite grains were chosen to make TEM foils in a FIB-SEM double beam system. One to three FIB slices for TEM analyses were then cut from the large antigorite flakes previously identified using SEM imaging. Each slice also contained other minerals and more than one grain of antigorite was present. In order to get newly grown and near equilibrium antigorite, the subhedral-euhedral coarse grains in the middle of the capsule were selected. The cross-sectional TEM (XTEM) specimens were prepared with a FEI Strata DB 235 scanning electron microscope/focused ion beam (FIB) system, in the Electron Microscopy Laboratory, Peking University, China. The FEI Strata DB235 is a dual beam SEM/FIB system combing a scanning electron microscope (SEM) with a thermal emission tip for high resolution imaging and a focused ion beam (FIB) with a gallium metal ion beam source for nanoscale cutting. The resolution of the high resolution SEM is ~3 nm.

TEM investigations for run D1512 were performed on a Hitachi H-9000NAR at 300 kV in the Electron Microscopy Laboratory, Peking University, China; and for the other samples (C4408, D1526, C4429 and C4442) were performed with a FEI Tecnai G2 F20 X-Twin transmission electron microscope with a FEG electron emitter at 200 kV, in the Electron Microscopy Laboratory, Peking University, China. An energy-dispersive X-ray analyser (EDAX) with ultrathin window was used for chemical analysis. The chemical composition was measured in scanning transmission (STEM) mode scanning the electron beam within a window. The magnification of the microscope was in the range of 50000-200000. Because antigorite is very sensitive to the electron beam (e.g. Mellini 1986, 1987; Wunder et al. 2001), when using such high magnification, the specimen was investigated under defocused beam conditions to reduce beam damage.

Two preparation techniques were used for the investigation of the natural sample from. The first one ("powder technique") consisted in grounding a small amount of sample C11107 in an agate mortar resulting in about 200 mesh powder; a small

amount of powder was added to deionized water to make a suspension. Then a copper mesh grid with a diameter of 1 mm was introduced into the suspension, parallel the surface of the liquid, thus collecting antigorite crystals preferentially oriented with their cleavage planes parallel to the main surface of the copper grid. This method maximises the observation of the *a* direction of antigorite at perpendicular to the electron beam. TEM investigations for Tianshan sample were performed on a Hitachi H-9000NAR at 300 kV in the Electron Microscopy Laboratory, Peking University, China.

The results from the "powder" technique were further compared with FIB prepared TEM foils from the same sample in order to investigate the effect of Al on the polysome *m* value. Three TEM foils (3.1D, 4.2H and 4.4H) representative of the two chemically distinct antigorite from this sample were prepared in the same FIB-SEM double beam system as described above and TEM investigations were performed at the same FEI Tecnai G2 F20 X-Twin transmission electron microscope with a FEG electron emitter at 200 kV.

The images acquired were analyzed by the Gatan DigitalMicrograph software to measure the length of the lattice fringe. Lattice-fringe micrographs of antigorite were obtained from *a* lattice modulation. The corresponding *m* value was determined from the lattice-fringe micrographs processed using the Gatan Digitalmicreograph (DM) software. A representative area (10 or 20 fringes) of an antigorite crystal without polysomatic disorder was selected using the DM software measurement tool to extract the width of the lattice fringes. The *d*-spacing of the *a* lattice fringe can then be determined after the amount of fringes within the selected area was counted. Finally, the *m* value was obtained by the equation of $m=(a/5.44)\times2+1$[*a* represents the length of *a*-axis; 5.44 Å is the length of sub-cells along *a*-axis (Uehara and Shirozu 1985; Uehara 1998)]. This method was performed on several antigorite grains in each sample in order to get statistically significant results. Diffraction patterns for antigorite were acquired for some samples but were not of good enough quality to get satisfactory results.

This is a preprint, the final version is subject to change, of the American Mineralogist (MSA)
Cite as Authors (Year) Title. American Mineralogist, in press.
DOI: https://doi.org/10.2138/am-2020-7159

RESULTS

Antigorite from the experimental charges

The conditions and the run products of the experiments are presented in Table 1. Antigorite is the main mineral coexisting with chlorite and olivine. Accessory Ti-chondrodite, Ti-clinohumite, ilmenite and Cr-spinel are additionally present (Fig. 2). In four runs: D1512 (620 °C, 25 kbar), C4408 (600 °C, 35 kbar), D1526 (650 °C, 30 kbar) and C4429 (650 °C, 35 kbar), antigorite reacted with brucite to form olivine and chlorite. Run C4442 (650 °C, 45 kbar) was close to the antigorite breakdown to form Ol+Opx+Chl+H_2O and abundant Opx was observed in this run (Figs. 2i,j).

Before the FIB extraction, each antigorite grain chosen (Fig. 2) was first characterized by Raman spectroscopy (Fig. 3). The main peaks in the spectra vary by up to two wavenumbers. No systematic relation of the shifts to P-T conditions could be established.

The average compositions of five grains in each run are reported in Table 2. The compositions of antigorite in the run products are only marginally different from the original starting antigorite (Al06-44), but the aluminium content consistently increases from 600-620 °C (2.67-2.78 wt. % Al_2O_3) to 650 °C (2.87-3.23 wt. % Al_2O_3) indicating antigorite recrystallization and composition adjustment with changing temperature conditions.

The TEM analyses showed that antigorite is the only serpentine variety in our high pressure and temperature experiments and no lizardite or chrysotile grains were observed. Antigorite shows a heterogeneous distribution of periodicities even on the same grain (Figs. 4a,c). Polysomatic disorder or modulation dislocations appear frequently (Figs. 4a,b and d). Antigorite intergrown with chlorite can be observed in several runs (Fig. 4c; Figs. 5a,c). The boundary between antigorite and chlorite is very clear in the TEM images. In run D1512, C4408 and D1526, this boundary is irregular. The lattice fringes change from the coarse fringes of antigorite to the fine fringes of chlorite and the *a* direction of antigorite is perpendicular to the *c* direction of chlorite

(Figs. 5a-c), indicating that the orientations of the tetrahedral-octahedral layers in the two minerals are aligned. The *m* values gradually decrease towards the boundary (Figs. 5a,c), reaching *m*=16 in run D1512 (620 ºC, 25 kbar) and *m*=14 in run D1526 (650 °C, 30 kbar) (Figs. 5a,e). This suggests reaction of antigorite to chlorite at the nanoscale in order to adjust the Al content as a function of changing pressure and temperature. In Fig. 5c, it can be seen clearly that the fringes of antigorite collapse and new chlorite fringes form. In run D1526 (650 °C, 30 kbar), TiCl lattice fringes are found in antigorite with *a* direction of antigorite parallel to the *c* direction of TiCl (Fig. 5d). The gradual transition and the alignment of crystallographic axes suggest that TiCl is a newly formed domain, coexisting with antigorite with an *m* value of 15 (Fig. 5d).

For each run, more than 40 data points were acquired and the periodicity distribution of antigorite was plotted in Fig. 6. In run D1512 (620 °C, 25 kbar), the peak *m* values are 17 and 18 (listed in decreasing abundance) among 57 data. For run C4408 (600 °C, 35 kbar) at higher pressures but slightly lower temperatures, the peak *m* values are 18, 17 and 19 among the 77 data. At 50 °C higher temperatures of run D1526 (650 °C, 30 kbar), the peak *m* values are lower with dominant values of 15 and 16 among 76 data. At the same temperature but higher pressures at 35 kbar in run C4429, the peak *m* values are 15, 16 and 17 among 40 data, and at 45 kbar in run C4442, the peak *m* values are 15, 17 and 16. Compared with D1526, it shows that the 15 kbar higher pressure results in *m* values that are slightly higher (Fig. 6f). The average of *a*-axis *d*-spacing shows clear changes among different runs, especially, there is a clear change between the low temperature runs at 620 °C and 600 °C (*m*=17-18) compared to the higher temperature runs at 650 °C (*m*=15-16; Fig. 6f). When all the data are plotted in a P-T diagram, a trend is visible. With increasing temperature, the *m* value decreases significantly as the antigorite breakdown reaction is approached (Fig. 7). On the other hand the *m* value increases only slightly (if any) over a relatively large pressure range (Fig. 7).

Tianshan antigorite

All the TEM results for Tianshan antigorite are plotted in Fig. 8. For the preparation as a powder, over 100 data points were acquired and the periodicity distribution of antigorite was plotted in Fig. 8a. The peak *m* value is 20, with a range between 19 and 21. This distribution corresponds to both UHP antigorite (low-Al) and HP-LP (high pressure to low pressure) antigorite (high-Al). In order to correlate textural and compositional differences in antigorite with *m* values, FIB samples of low-Al and high-Al antigorite were additionally investigated. The orientation of two of the FIB samples allowed a clear characterization of the *a* direction antigorite (3.1D and 4.2H), whereas for 4.4H only the *c* direction could be determined. For 3.1D (low-Al antigorite with Al_2O_3=1.11 wt.% included in Ti-chondrodite), the peak *m* values are 21, 20 among the 36 data (Fig. 8b). The high-Al antigorite from the matrix (4.2H) with Al_2O_3=3.38 wt.% has a sharp peak *m* value of 19 among the 33 data (Fig. 8c). The higher *m* values of the low-Al antigorite is consistent with its UHP and relatively low temperature conditions of equilibration, which is in accordance with the experimental results. Crystal defects such as polysomatic disorder, modulation dislocations and offset are commonly observed (Figs. 9a-c). In the high-Al antigorite (4.2H and 4.4H), chlorite inclusions are found in antigorite (Figs. 9d,e), or chlorite intergrown with antigorite (Fig. 9f). This suggests that antigorite decomposition most likely continued during the final stages of cooling during exhumation (marked by a decrease in Al-content) but it cannot be detected by microprobe analyses as the analysed volume is much larger than the size of the chlorite intergrowths.

DISCUSSION

Approach to equilibrium in the experiments

Ulmer and Trommsdorff (1995) mentioned that the structural state of antigorite used for the experiments might have an important influence on its stability. The starting

antigorite used in our experiments comes from Cerro del Almirez ultramafic massif, which is an example of high pressure and high temperature antigorite serpentinites (Trommsdorff et al., 1998). The chosen starting antigorite for the experiments (Al06-44) is equivalent to the sample Al06-46 that was previously characterized by TEM (Padrón-Navarta et al. 2008). It mostly consists of the polysome *m*=16 with a less abundant *m*=15. This sample outcrops less than a meter from the reaction front in Cerro del Almirez and thus equilibrated at T of 680 °C and P of 16-19 kbar (Padrón-Navarta et al. 2010). It is more disordered (i.e. containing pervasive twins and some reaction rims) than other serpentinite far from the reaction front that are characterized by a polysome *m*=17 and almost no structural defects. We selected the sample for the starting material of this study with more structural defects with the aim to enhance the kinetics of the recrystallization. There are several indications that the experiments attained equilibrium with respect to the main mineral assemblage. The added brucite reacted completely with antigorite to produce new olivine and chlorite. The presence of such chlorite and olivine means that the Al-content of antigorite is nominally buffered in all experiments. The onset of antigorite breakdown to orthopyroxene+olivine+chlorite observed at 650 °C, 45 kbar is in excellent agreement with the study of Ulmer and Trommsdorff (1995) also using a natural starting material (Fig. 1; Shen et al. 2015). The minor minerals Ti-chondrodite and Ti-clinohumite did not fully equilibrate, but they are known to be sluggish in their reactions (Shen et al. 2015). The intergrowth of Ti-clinohumite and antigorite at the nanoscale (Fig. 5d) suggests reaction of ilmenite+antigorite to form new clinohumite. This observation indicates that the stability field of antigorite+olivine+Ti-clinohumite extends to at least to 30 kbar, 650 °C.

It is more difficult to establish to what extent the starting material antigorite has approached equilibrium at the different conditions investigated. The quantitative analyses showed that the Al-content of antigorite, which is buffered by the assemblage, changes with changing pressure and temperature, consistent with thermodynamic calculations (Padrón-Navarta et al. 2013). However, the extent of change is rather smaller than expected. This can be explained by the TEM

observations of chlorite intergrowth with antigorite suggesting adjustment of Al content in antigorite at the nanoscale. The excitation volume of the SEM and EPMA analyses (1-2 µm diameter) will always be bigger than this intergrowth, indicating the Al-in-antigorite measurements represent mixed analyses of antigorite and included chlorite. The TEM observations also show that the *m* values change between starting material and run conditions. Although variations are observed in a single sample, the statistical distribution of the systematic change of *m* with P and T provides further evidence for approach towards equilibrium.

Comparison with previous experiments

In a pioneering study, Wunder et al. (2001) combined experiments with a TEM study to show a systematic variation of *m* values from 13 to 23 with changes in pressure and temperature in the synthetic MSH-system. They observed that the *m*-isolines have a steep positive slope in P-T space and that the spacing of isolines is getting narrower as the antigorite breakdown curve is approached. The lowest *m* value of 14 was observed where the antigorite breakdown curve changes from a positive to a negative slope. The same features have also been observed in our study using natural starting materials (Fig. 7). It is interesting to note that the introduction of Al into the system creates some important differences. The first important change is an increased stability field of Al-bearing antigorite by 40-60 °C when the antigorite breakdown curve of Wunder and Schreyer (1997) in the MSH system is compared to the results of Ulmer and Trommsdorff (1995), Bromiley and Pawley (2003) and Padrón-Navarta et al. (2010) using a natural antigorite. It has been noted that a few weight percent of Al_2O_3 into antigorite can stabilize it to significantly higher temperatures and pressures (Bromiley and Pawley 2003). The effect of Al on the stability of antigorite has been quantified by a new thermodynamic model that allows calculation of compositional isopleths in pseudosections (Padrón-Navarta et al. 2013). The main question is how the incorporation of Al influences the *m* values of antigorite. Because of the higher thermal stability of Al-bearing antigorite, experiments could be conducted at higher

temperatures in this study compared to the study of Wunder et al. (2001). As a result the distribution of *m* values of a single experiment is tighter in this study. The second important point is that the *m* values for a given P-T are higher in this study compared to the values of Wunder et al (2001). For example at 600 °C, 35 kbar the *m* value in our study is 18 whereas in the MSH system it is only 15. It appears that the incorporation of Al into antigorite has a similar effect on the *m* value as on the stability field. This means that essentially the whole topology of the MSH-diagram is shifted to higher temperatures by 50-100 °C in the natural system (Fig. 10). At the antigorite breakdown, an *m* value of 14 is reached in the natural antigorite as well as in the MSH antigorite, indicating that this represents a critical limit for the antigorite structure. The *m*-isolines are tighter spaced in the natural antigorite, meaning that higher *m* values ($m>20$) can be reached in low temperature, high-pressure antigorite serpentinites. The effect of Fe on the stability of antigorite is twofold. The presence of ferrous iron results in a decrease of the antigorite stability field by up to 20 °C depending on the reactive bulk composition (Padrón-Navarta et al. 2010; Bretscher et al. 2018). On the other hand, ferric iron substitutes for Al and thus will stabilize antigorite to higher temperatures (Padrón-Navarta et al. 2013). Assuming a maximum amount of 50% of ferric iron in antigorite close to its breakdown (Debret et al., 2015) results in a Fe^{3+} of maximal 1/3 of the total trivalent cations. Therefore, the effect of Fe is subordinate to the effect of Al on the stability of antigorite. The impact of this amount of Fe^{3+} on *m* values in antigorite and whether there is a systematic change of *m* values at constant Al-contents but changing Fe^{3+} contents requires further investigation.

Low temperature UHP antigorite

Our experimental samples cover the temperature range of 600-650 °C at pressures of 25-45 kbar. It would have been desirable to conduct additional experiments at 35 kbar in order to evaluate *m* values at UHP conditions at temperatures below 600 °C. However, as the reaction kinetics will get slower, the re-adjustment of the natural

starting material to changing pressure and temperature conditions will be more and more sluggish. For this reason we opted to an alternative approach to investigate in detail antigorite from a natural sample that experienced UHP metamorphism. The TiCh/TiCl bearing serpentinized wehrlite from southwestern Tianshan (China) experienced UHP metamorphism at 520±10 °C, 37±7 kbar (Shen et al. 2015). TEM studies on this antigorite showed two main features. Firstly, the significantly lower temperatures of 520 °C resulted in *m* values that range from 18-22 in the powder sample, clearly lower than the experimental samples equilibrated at higher temperature. Secondly, the FIB-TEM sample showed a clear distinction in *m* values between low-Al antigorite (*m*=20-21) that formed at peak pressure conditions and high-Al antigorite (*m*=19) that formed at similar temperatures but much lower pressures of 10-20 kbar. Together with the experimental data, these observations provide evidence that *m* values are increasing with decreasing temperature but increasing with decreasing pressure.

An inferred P-T-*m* diagram for natural antigorite

In this section we now compare and combine data from our study with TEM studies of natural antigorite with known P-T conditions in order to get a more comprehensive P-T-*m* diagram for natural antigorite (Fig. 10).

(1) The notable sample MG159 from Franscia, Val Malenco (Northern Italy), which was first studied by Trommsdorff and Evans (1972), is especially homogeneous both texturally and crystallographically. Antigorite contains 1.39 wt.% Al_2O_3 and 2.65 wt.% FeO (Padrón-Navarta et al. 2008) and formed at 435±30 °C, ~5 kbar (Trommsdorff and Evans 1980; Mellini et al. 1987). It displays an unusually regular *m*=17 (Mellini et al. 1987). (2) Antigorite from a chl-serpentinite with 2.73 wt.% Al_2O_3 and 3.98 wt.% FeO is at the antigorite-out reaction (Padrón-Navarta et al., 2008) and has *m* down to 14-15, with abundant structural disorder features, such as pervasive twins and reaction rims. On the other hand, antigorite away from the reaction front has *m*=17 (Padrón-Navarta et al. 2008) at P-T conditions of 640 °C,

17-20 kbar (Trommsdorff et al. 1998; López Sánchez-Vizcaíno et al. 2005). (3) Serpentinite from Escambray massif, Central Cuba have preserved high-grade structures with P>12 kbar and T> 450 °C determined by associated eclogites (e.g. Spear 1993; Auzende et al. 2002). The antigorite from this serpentinite has a modulation wavelength of 37 Å and 40 Å (Auzende et al. 2002), which corresponds to *m*=15-16 using our calculation method with the antigorite composition of 2.7-3.5 wt.% Al_2O_3 and 3.6-4.3 wt.% FeO (Auzende et al. 2002); (4) Serpentinite samples from the Monviso (Western Alps, Italy) were studied with TEM from three different locations (Auzende et al. 2006). Serpentinites from Passo Gallarino (PG) and Viso Mozzo (VM) have relatively narrow P-T conditions of 12-13 kbar, 450±40 °C and are associated with eclogites (Schwartz et al. 2001). The antigorite displays peak *m* values of 18-19 (Auzende et al. 2006). A serpentinite sample from Lago Superiore (LS) records higher P-T conditions ranging from 19±2 kbar, 580±40 °C (Schwartz et al. 2001) up to >24 kbar, 620±50 °C (Messiga et al. 1999), and the measured peak *m* value is 19. The Monviso antigorites contain about 2-3 wt.% Al_2O_3 and 3-4 wt.% FeO_t (Auzende et al. 2006). When we combine our experimental data and Tianshan natural data at high pressures with these data from the literature at lower pressures, a completely contoured antigorite stability field can be established. The slope of the *m*-isolines becomes steeper when pressure is above 20 kbar. The *m* value of antigorite is thus controlled by both temperature and pressure at lower pressure (< 20 kbar), and mainly by temperature at high pressure. The contoured *m*-isolines thus mimic to some extent the antigorite stability (Fig. 1). Especially the positive slope up to 20 kbar is approximately parallel to the antigorite breakdown reaction. At higher pressures, however, the antigorite breakdown reaction has a steep negative slope whereas the *m*-isolines display a steep positive slope.

The potential use of such a P-T-*m* diagram can be shown from a case study of the Western Alps, where serpentinites underwent a full subduction-exhumation cycle. Antigorite serpentinites from Erro Tobbio in the Voltri massif (Ligurian Alps, Italy) have preserved four stages of metamorphism: a prograde subduction stage I/II recorded at 7-14 kbar, 310-490 °C; a peak stage III recorded at 16-22 kbar,

520-620 °C; and an exhumation stage IV recorded at 13-21 kbar, 500-620 °C (Hermann et al. 2000). TEM studies suggested that stage I/II antigorite have a range of *m* values of 18, 19, 20, 21, without any peak *m* value, consistent with a low temperature of equilibration. Particularly the *m* value of 21 is interesting as this is a clear indication for a low temperature-high pressure equilibration. Stage III antigorite have *m* values of 17, 19 more frequently than 16, 18, 20 in good agreement with the inferred peak P-T conditions. The relatively large spread of *m* values, however, indicates that full equilibration of antigorite is not achieved even for samples that reached up to 600 °C, experienced deformation and where exposed to these conditions for geologic timescales. Stage IV antigorite show most abundant *m* values of 20, 19, indicating that the *m* value obtained during peak conditions is partly reset during retrograde deformation and equilibration (Auzende et al. 2006).

Water content variation during antigorite dehydration

Antigorite has an ideal structural formula of $Mg_{3m-3}Si_{2m}O_{5m}(OH)_{4m-6}$ in the MSH system, and the variation of the *m* value will change the composition of antigorite. In particular, Wunder et al. (2001) showed that the observed decrease of the *m* values with increasing temperature corresponds to a dehydration reaction of the generalised form:

antigorite (high *m*) →antigorite (low *m*) + olivine + H_2O (1)

As a consequence small amounts of free fluid are present during the prograde metamorphism of antigorite serpentinites. Padrón-Navarta et al. (2013) have shown that also the increasing incorporation of Al in antigorite during prograde metamorphism will lead to a small amount of fluid release through a continuous reaction involving also chlorite and olivine. Padrón-Navarta et al. (2013) have shown that about 0.1 wt.% H_2O is liberated during prograde metamorphism in the chlorite-olivine-antigorite stability field from ~530-650 °C, 30 kbar. With our new data we can now assess the contributions of the change in *m* value to the continuous water liberation in subducted antigorite serpentinites. In order to calculate the

theoretical water content variation as a function of *m* values in antigorite, we use the general formula $Mg_{3m-3-y}Si_{2m-y}Al_{2y}O_{7m-3}(H_2O)_{2m-3}$ (*m* is the number of tetrahedral in a single chain, that is the *m* value of antigorite; 2*y* represents the content of Al replacing Mg and Si) as antigorite formula. A range of *m* values from 14-20, and Al-contents y=1 (corresponding to Al_2O_3 content of 2.73 wt. %). The calculated water content is in the range of 12.41-12.14 (Fig. 11) indicating that the fluid release from change in *m* value is about double that of the change in Al-content. The tight spacing of the *m*-isolines towards the antigorite breakdown reaction (Fig. 10) thus will result in continuous fluid production. Therefore, serpentinites will deform during prograde subduction zone conditions in the presence of small amounts of fluid (Wunder et al. 2001) thus activating dissolution-precipitation creep mechanisms in addition to dislocation creep (Padrón-Navarta et al. 2012, 2013).

IMPLICATIONS

1) Antigorite is arguably the most important water carrier in subduction zones (e.g. Ulmer and Trommsdorff 1995; Wunder and Schreyer 1997; Trommsdorff et al. 1998; Wunder et al. 2001; Scambelluri et al. 2001, 2004a, b, 2014; Hattori and Guillot 2003, 2007; Rüpke et al. 2004; Garrido et al. 2005; Alt et al. 2012; Padrón-Navarta et al. 2011, 2013, 2015, Maurice et al., 2018). Reconstruction of P-T paths in serpentinites from former subduction zones is an important way to gain insights into subduction dynamics. However, due to the large stability field of antigorite it is extremely difficult to retrieve P-T conditions from antigorite serpentinites. We have shown that the *m* value of natural antigorite changes systematically with pressure and temperature and thus can potentially be used in future studies to constrain the metamorphic evolution of serpentinites.

2) There has been wide interest in the *in-situ* major and trace element systematics of serpentinites (e.g. Garrido et al. 2005; Deschamps et al. 2010, 2011, 2013; Kodolányi et al. 2011; Debret et al. 2013; Marchesi et al. 2013; Peters et al. 2017).

Our TEM study shows that there exist interlayers of Ti-clinohumite and chlorite with antigorite at the nanoscale. Additionally, full equilibration to a single *m* value is rather rare. Electron microprobe analyses (with 1-5 μm resolution) and laser-ablation analyses (with spot size ranging typically from 15-60 μm) will inevitably integrate such heterogeneity. These observations indicate that extreme care has to be taken for the interpretation of major and trace element compositions of antigorite as it could represent a composite signal that has been acquired during multiple stages of the evolution of the serpentinites.

3) Serpentinites are important for lubrication of the plate interface between subducted slab and the mantle wedge up to the decoupling point at about 60-80 km depth (e.g., Iwamori and Zhao 2000; Hyndman and Peacock 2003; Hattori and Guillot 2003, 2007; Kawakatsu and Watada 2007; Syracuse et al. 2010; Padrón-Navarta et al., 2012). Our study of natural antigorite shows that the *m* value is decreasing gradually from ~ 21 at the lizardite to antigorite transition to ~14 at the antigorite breakdown. This change in *m* value causes a continuous dehydration. The presence of small amounts of pore fluids might have important implications for the deformation behaviour of antigorite. There is a current controversy about the active deformation mechanism of antigorite at subduction zone conditions. Proposed mechanisms range from either dominated by dislocation creep (Hilairet et al. 2007), dissolution precipitation creep (Auzende et al. 2006; Wassmann et al. 2011) or both (Padrón-Navarta et al. 2012). Prograde deformation will take place at water-present conditions and influence deformation if the active deformation mechanism for natural strain rates is accommodated by dissolution precipitation processes (akin to dissolution precipitation creep). On the other hand, the continuous generation of modulation dislocations (intracrystalline defects generated at the boundary of two polysomes) along a prograde path will also enhance dislocation creep by increasing other non-basal glide systems (Padrón-Navarta et al. 2012; Amiguet et al. 2012, 2014).

ACKNOWLEDGMENTS AND FUNDING

This study was supported by the National Natural Science Foundation of China (Nos. 41872067, 41572051, 41972064 41630207, 41703053, 41720104009, 41802070), Project of China Geological Survey (No. DD20190006) and Foundation of Chinese Academy of Geological Sciences (Nos. J1701, YYWF201702). We thank the China Scholarship Council for supporting the 12-month visit of T. T. Shen at RSES, The Australian National University. We would like to thank M. Mellini and an anonymous reviewer and editor T. Müller for constructive comments that helped to improve the paper.

REFERENCES CITED

Alt, J.C., Garrido, C.J., Shanks, W.C., Turchyn, A., Padrón-Navarta, J.A., López Sánchez-Vizcaíno, V., Gómez Pugnaire, M.T., and Marchesi, C. (2012) Recycling of water, carbon, and sulfur during subduction of serpentinites: A stable isotope study of Cerro del Almirez, Spain. Earth and Planetary Science Letters, 327-328, 50-60.

Amiguet, E., Reynard, B., Caracas, R., Van de Moortèle, B., Hilairet, N., and Wang, Y. (2012) Creep of phyllosilicates at the onset of plate tectonics. Earth and Planetary Science Letters, 345-348, 142-150.

Amiguet, E., Van De Moortèle, B., Cordier, P., Hilairet, N., and Reynard, B. (2014) Deformation mechanisms and rheology of serpentines in experiments and in nature. Journal of Geophysical Research: Solid Earth, 119(6), 4640-4655.

Aruja, E. (1944) An X-ray study of the crystal structure of antigorite. Mineralogical Magazine, 27, 65-74.

Auzende, A., Devouard, B., Guillot, S., Daniel, I., Baronnet, A., and Lardeaux, J.M. (2002) Serpentinites from Central Cuba: petrology and HRTEM study. European Journal of Mineralogy, 14, 905-914.

Auzende, A., Guillot, S., Devouard, B., and Baronnet, A. (2006) Serpentinites in an

Alpine convergent setting: effects of metamorphic grade and deformation on microstructures. European Journal of Mineralogy, 18, 21-33.

Bebout, G.E., Bebout, A.E., and Graham, C.M. (2007) Cycling of B, Li, and LILE (K, Cs, Rb, Ba, Sr) into subduction zones: SIMS evidence from micas in high-P/T metasedimentary rocks. Chemical Geology, 239, 284-304.

Bezacier, L., Reynard, B., Cardon, H., Montagnac, G., and Bass, J.D. (2013) High-pressure elasticity of serpentine and seismic properties of the hydrated mantle wedge. Journal of Geophysical Research: Solid Earth, 118, 527-535, doi:10.1002/jgrb.50076.

Bonatti, E., and Crane, K. (1984) Oceanic Fracture Zones. Scientific American, 250, 40-51.

Bose, K., and Navrotsky, A. (1998) Thermochemistry and phase equilibria of hydrous phases in the system MgO-SiO_2-H_2O: Implications for volatile transport to the mantle. Journal of Geophysical Research, 103, 9713-9719.

Bretscher, A., Hermann, J., and Pettke, T. (2018) The influence of oceanic oxidation on serpentinite dehydration during subduction. Earth and Planetary Science Letters, 499, 173-184.

Bromiley, G.D., and Pawley, A.R. (2003) The stability of antigorite in the systems MgO-SiO_2-H_2O (MSH) and MgO-Al_2O_3-SiO_2-H_2O. American Mineralogist, 88, 99-108.

Capitani, G., and Mellini, M. (2004) The modulated crystal structure of antigorite; the m = 17 polysome. American Mineralogist, 89, 147-158.

Capitani, G., and Mellini, M. (2006) The crystal structure of a second antigorite polysome (m=16), by single-crystal synchrotron diffraction. American Mineralogist, 91, 394-399.

Chen, L., Xu, J., and Chen, J. (2015) Applications of scanning electron microscopy in earth sciences. Science China: Earth Sciences, 58, 1768-1778, doi: 10.1007/s11430-015-5172-9.

Debret, B., Andreani, M., Godard, M., Nicollet, C., Schwartz, S., and Lafay, R. (2013) Trace element behavior during serpentinization/de-serpentinization of an

626 eclogitized oceanic lithosphere: A LA-ICPMS study of the Lanzo ultramafic
627 massif (Western Alps). Chemical Geology, 357, 117-133.
628 Debret, B., Bolfan-Casanova, N., Padrón-Navarta, J.A., Martin-Hernandez, F.,
629 Andreani, M., Garrido, C.J., López Sánchez-Vizcaíno, V., Gómez-Pugnaire, M.T.,
630 Muñoz, M., and Trcera, N. (2015) Redox state of iron during high-pressure
631 serpentinite dehydration. Contributions to Mineralogy and Petrology, 169.
632 Deschamps, F., Guillot, S., Godard, M., Chauvel, C., Andreani, M., and Hattori, K.
633 (2010) In situ characterization of serpentinites from forearc mantle wedges: timing
634 of serpentinization and behavior of fluid-mobile elements in subduction zones.
635 Chemical Geology, 269, 262-277.
636 Deschamps, F., Guillot, S., Godard, M., Andreani, M., and Hattori, K. (2011)
637 Serpentinites act as sponges for fluid-mobile elements in abyssal and subduction
638 zone environments. Terra Nova, 23, 171-178.
639 Deschamps, F., Godard, M., Guillot, S., Chauvel, C., Andreani, M., Hattori, K.,
640 Wunder, B. and France, L. (2012) Behavior of fluid-mobile elements in
641 serpentines from abyssal to subduction environments: Examples from Cuba and
642 Dominican Republic. Chemical Geology, 312-313, 93-117.
643 Deschamps, F., Godard, M., Guillot, S., and Hattori, K. (2013) Geochemistry of
644 subduction zone serpentinites: A review. Lithos, 178, 96-127.
645 Evans, B.W., Johannes, W., Oterdoom, H., and Tommsdorff, V. (1976) Stability of
646 crysotile and antigorite in the serpentinite multisystem. Schweizerische
647 Mineralogische und Petrographische Mitteilungen, 56, 79-93.
648 Evans, B.W. (2004) The serpentinite multisystem revisited: chrysotile is metastable.
649 International Geology Review, 46, 479-506.
650 Evans, B.W., Hattori, K., and Baronnet, A. (2013) Serpentinite: What, Why, Where?
651 Elements, 9, 99-106.
652 Frost, B.R. (1975) Contact metamorphism of serpentinite, chloritic blackwall and
653 rodingite at Paddy-Go-Easy Pass, Central Cascades, Washington. Journal of
654 Petrology, 16, 272-313.
655 Garrido, C.J., López Sánchez-Vizcaíno, V., Gómez-Pugnaire, M.T., Trommsdorff, V.,

Alard, O., Bodinier, J.L., and Godard, M. (2005) Enrichment of HFSE in chlorite-harzburgite produced by high-pressure dehydration of antigorite-serpentinite: Implications for subduction magmatism. Geochemistry, Geophysics, Geosystems, 6, 6: Q01J15. doi:10.1029/2004GC000791.

Ghaderi, N., Zhang, H., and Sun, T. (2015) Relative stability and contrasting elastic properties of serpentine polymorphs from first-principles calculations. Journal of Geophysical Research: Solid Earth, 120, 4831-4842.

Harvey, J., Garrido, C.J., Savov, I., Agostini, S., Padrón-Navarta, J.A., Marchesi, C., López Sánchez-Vizcaíno, V., and Gómez-Pugnaire, M.T. (2014) ^{11}B-rich fluids in subduction zones: The role of antigorite dehydration in subducting slabs and boron isotope heterogeneity in the mantle. Chemical Geology, 376, 20-30.

Hattori, K.H., and Guillot, S. (2003) Volcanic fronts form as a consequence of serpentinite dehydration in the forearc mantle wedge. Geology, 31, 525–528.

Hattori, K.H., and Guillot, S. (2007) Geochemical character of serpentinites associated with high- to ultrahigh-pressure metamorphic rocks in the Alps, Cuba, and the Himalayas: recycling of elements in subduction zones. Geochemistry, Geophysics, Geosystems, 8, http://dx.doi.org/10.1029/2007GC001594.

Hermann, J., Müntener, O., and Scambelluri, M. (2000) The importance of serpentine mylonites for subduction and exhumation of oceanic crust. Tectonophysics, 327, 225-238.

Hermann, J., Rubatto, D., and Trommsdorff, V. (2006) Sub-solidus Oligocene zircon formation in garnet peridotite during fast decompression and fluid infiltration (Duria, Central Alps). Mineralogy and Petrology, 88, 181-206.

Hilairet, N., Daniel, I., and Reynard, B. (2006) Equation of state of antigorite, stability field of serpentines, and seismicity in subduction zones. Geophysical Research Letters, 33, L02302, doi:10.1029/2005GL024728.

Hilairet, N., Reynard, B., Wang, Y.B., Daniel, I., Merkel, S., Nishiyama, N., and Petitgirard, S. (2007) High-pressure creep of serpentine, interseismic deformation, and initiation of subduction. Science, 318, 1910-1913.

Iwamori, H., and Zhao, D. (2000) Melting and seismic structure beneath the northeast

686 Japan arc. Geophysical Research Letters, 27, 425-428.
687 Jahanbagloo, C., and Zoltai, T. (1968) The crystal structure of a hexagonal
688 Al-serpentine. American Mineralogist, 53, 14-24.
689 Janecky, D.R., and Seyfried, W.E. (1986) Hydrothermal serpentinization of peridotite
690 within the oceanic crust: Experimental investigations of mineralogy and major
691 element chemistry. Geochimica et Cosmochimica Acta, 50, 1357-1378.
692 Kawakatsu, H., and Watada, S. (2007) Seismic evidence for deep-water transportation
693 in the mantle. Science, 316, 1468-1471.
694 Kodolányi, J., and Pettke, T. (2011) Loss of trace elements from serpentinites during
695 fluid-assisted transformation of chrysotile to antigorite — An example from
696 Guatemala. Chemical Geology, 284, 351-362.
697 Kunze, V.G. (1961) Antigorit. Strukturtheoretische Grundlagen und ihre praktische
698 Bedeutung fdr die weitere Serpentin-Forschung. Fortschr. Mineral. 39, 206-324.
699 López Sánchez-Vizcaíno, V., Trommsdorff, V., Gómez-Pugnaire, M.T., Garrido, C.J.,
700 Müntener, O., and Connolly, J.A.D. (2005) Petrology of titanian clinohumite and
701 olivine at the high-pressure breakdown of antigorite serpentinite to chlorite
702 harzburgite (Almirez Massif, S. Spain). Contributions to Mineralogy and
703 Petrology, 149, 627-646.
704 Marchesi, C., Garrido, C.J., Padrón-Navarta, J.A., López Sánchez-Vizcaíno, V., and
705 Gómez-Pugnaire, M.T. (2013) Element mobility from seafloor serpentinization to
706 high-pressure dehydration of antigorite in subducted serpentinite: Insights from
707 the Cerro del Almirez ultramafic massif (southern Spain). Lithos, 178, 128-142.
708 Maurice, J., Bolfan-Casanova, N., Padrón-Navarta, J.A., Manthilake, G., Hammouda,
709 T., Hénot, J.M., Andrault, D., 2018. The stability of hydrous phases beyond
710 antigorite breakdown for a magnetite-bearing natural serpentinite between 6.5 and
711 11 GPa. Contrib. Mineral. Petrol. 173, 86.
712 Mellini, M. (1986) Chrysotile and polygonal serpentine from the Balangero
713 serpentinite. Mineralogical Magazine, 50, 301-306.
714 Mellini, M., Trommsdorff, V., and Compagnoni, R. (1987) Antigorite polysomatism:
715 Behaviour during progressive metamorphism. Contributions to Mineralogy and

716 Petrology, 97, 147-155.
717 Messiga, B., Kienast, J.R., Rebay, G., Riccardi, P., and Tribuzio, R. (1999) Cr rich
718 magnesiochloritoïd eclogites from the Monviso ophiolites (Western Alps, Italy).
719 Journal of Metamorphic Geology, 17, 287-299.
720 Nestola, F., Angel, R.J., Zhao, J., Garrido, C.J., Sánchez-Vizcaíno, V.L., Capitani, G.,
721 and Mellini, M. (2010) Antigorite equation of state and anomalous softening at 6
722 GPa: an in situ single-crystal X-ray diffraction study. Contributions to Mineralogy
723 and Petrology, 160, 33-43.
724 Padrón-Navarta, J.A., and Hermann, J. (2017) A subsolidus olivine water solubility
725 equation for the Earth's upper mantle. Journal of Geophysical Research: Solid
726 Earth, 122, 9862-9880. https://doi.org/10.1002/2017JB014510.
727 Padrón-Navarta, J.A., López Sánchez-Vizcaíno, V., Garrido, C.J., Gómez-Pugnaire,
728 M.T., Jabaloy, A., Capitani, G., and Mellini, M. (2008) Highly ordered antigorite
729 from Cerro del Almirez HP–HT serpentinites, SE Spain. Contributions to
730 Mineralogy and Petrology, 156, 679-688.
731 Padrón-Navarta, J.A., Hermann, J., Garrido, C.J., López Sánchez-Vizcaíno, V., and
732 Gómez-Pugnaire, M.T. (2010) An experimental investigation of antigorite
733 dehydration in natural silica-enriched serpentinite. Contributions to Mineralogy
734 and Petrology, 159, 25-42.
735 Padrón-Navarta, J.A., López Sánchez-Vizcaíno, V., Garrido, C.J., and
736 Gómez-Pugnaire, M.T. (2011) Metamorphic record of high-pressure dehydration
737 of antigorite serpentinite to chlorite harzburgite in a subduction setting (Cerro del
738 Almirez, Nevado-Filabride Complex, Southern Spain). Journal of Petrology, 52,
739 2047-2078.
740 Padrón-Navarta, J.A., Tommasi, A., Garrido, C.J., and López Sánchez-Vizcaíno, V.
741 (2012) Plastic deformation and development of antigorite crystal preferred
742 orientation in high-pressure serpentinites. Earth and Planetary Science Letters,
743 349-350, 75-86.
744 Padrón-Navarta, J.A., López Sánchez-Vizcaíno, V., Hermann, J., Connolly, J.A.D.,
745 Garrido, C.J., Gómez-Pugnaire, M.T., and Marchesi, C. (2013) Tschermak's

substitution in antigorite and consequences for phase relations and water liberation in high-grade serpentinites. Lithos, 178, 186-196.

Padrón-Navarta, J.A., Tommasi, A., Garrido, C.J., and Mainprice, D. (2015) On topotaxy and compaction during antigorite and chlorite dehydration: an experimental and natural study. Contributions to Mineralogy and Petrology, 169, 35. doi 10.1007/s00410-015-1129-4.

Pawley, A. (2000) Stability of clinohumite in the system MgO-SiO_2-H_2O. Contributions to Mineralogy and Petrology, 138, 284-291.

Perrillat, J., Daniel, I., Koga, K., Reynard, B., Cardon, H., and Crichton, W. (2005) Kinetics of antigorite dehydration: A real-time X-ray diffraction study. Earth and Planetary Science Letters, 236, 899-913.

Peters, D., Bretscher, A., John, T., Scambelluri, M., and Pettke, T. (2017) Fluid-mobile elements in serpentinites: Constraints on serpentinisation environments and element cycling in subduction zones. Chemical Geology, 466, 654-666.

Reynard, B., and Wunder, B. (2006) High-pressure behavior of synthetic antigorite in the MgO-SiO_2-H_2O system from Raman spectroscopy. American Mineralogist, 91, 459-462.

Rüpke, L.H., Morgan, J.P., Hort, M., and Connolly, J.A.D. (2004) Serpentine and the subduction zone water cycle. Earth and Planetary Science Letters, 223, 17-34.

Savov, I.P., Ryan, J.G., D'Antonio, M., Kelley, K., and Mattie, P. (2005) Geochemistry of serpentinized peridotites from the Mariana fore-arc Conical Seamount, ODP Leg 125: implications for the elemental recycling at subduction zones. Geochemistry, Geophysics, Geosystems, 6, 1-24.

Scambelluri, M., Rampone, E., and Piccardo, G.B. (2001) Fluid and element cycling on subducted serpentinite: a trace-element study of the Erro-Tobbio high-pressure ultramafites (Western Alps, NW Italy). Journal of Petrology, 42, 55-67.

Scambelluri, M., Fiebig, J., Malaspina, N., Müntener, O., and Pettke, T. (2004a) Serpentinite Subduction: Implications for Fluid Processes and Trace-Element Recycling. International Geology Review, 46, 595-613.

Scambelluri, M., Müntener, O., Ottolini, L., Pettke, T.T., and Vannucci, R. (2004b)

776 The fate of B, Cl and Li in the subducted oceanic mantle and in the antigorite
777 breakdown fluids. Earth and Planetary Science Letters, 222, 217-234.
778 Scambelluri, M., Pettke, T., Rampone, E., Godard, M., and Reusser, E. (2014)
779 Petrology and trace element budgets of high-pressure peridotites indicate
780 subduction dehydration of serpentinized mantle (Cima di Gagnone, Central Alps,
781 Switzerland). Journal of Petrology, 55, 459-498.
782 Scambelluri, M., Cannaò, E., and Gilio, M. (2019) The water and fluid-mobile
783 element cycles during serpentinite subduction. A review. European Journal of
784 Mineralogy, https://doi.org/10.1127/ejm/2019/0031-2842. Schwartz, S., Allemand,
785 P., and Guillot, S. (2001) Numerical model of effect of serpentinites on the
786 exhumation of eclogitic rocks: insights from the Monviso ophiolitic massif
787 (Western Alps). Tectonophysics, 342, 193-206.
788 Schwartz, S., Guillot, S., Reynard, B., Lafay, R., Debret, B., Nicollet, C., Lanari, P.,
789 and Auzende, A.L. (2013) Pressure-temperature estimates of the
790 lizardite/antigorite transition in high pressure serpentinites. Lithos, 178, 197-210.
791 Schmidt, M.W., and Poli, S. (1998) Experimentally based water budgets for
792 dehydrating slabs and consequences for arc magma generation. Earth and
793 Planetary Science Letters, 163, 361-379.
794 Scicchitano, M.R., Rubatto, D., Hermann, J., Shen, T.T., Padrón-Navarta, J.A.,
795 Williams, I.S., and Zheng, Y.F. (2018) *In situ* oxygen isotope determination in
796 serpentine minerals by ion microprobe: reference materials and applications to
797 ultrahigh-pressure serpentinites. Geostandards and Geoanalytical Research,
798 https://doi.org/10.1111/ggr.12232.
799 Shen, T.T., Hermann, J., Zhang, L.F., Padrón-Navarta, J.A., and Chen, J. (2014) FTIR
800 spectroscopy of Ti-chondrodite, Ti-clinohumite, and olivine in deeply subducted
801 serpentinites and implications for the deep water cycle. Contributions to
802 Mineralogy and Petrology, 167, 992.
803 Shen, T.T., Hermann, J., Zhang, L.F., Lü, Z., Padrón-Navarta, J.A., Xia, B., and Bader,
804 T. (2015) UHP Metamorphism Documented in Ti-chondrodite- and
805 Ti-clinohumite-bearing Serpentinized Ultramafic Rocks from Chinese

Southwestern Tianshan. Journal of Petrology, 56, 1425-1458.

Shen, T.T., Zhang, L.F., and Chen, J. (2016) Metamorphism of subduction zone serpentinite. Acta Petrologica Sinica, 32, 1206-1218 (in Chinese with English abstract).

Spear, F.S. (1993) Metamorphic Phase Equilibria and Pressure- Temperature-Time Paths. Mineral. Soc. Am., Mon. Ser., 799.

Syracuse, E.M., van Keken, P.E., and Abers, G.A. (2010) The global range of subduction zone thermal models. Physics of the Earth and Planetary Interiors, 183, 73-90.

Thompson, J.B. Jr. (1978) Biopyriboles and polysomatic series. American Mineralogist, 63, 239-249.

Trommsdorff, V., and Evans, B.W. (1972) Progressive metamorphism of antigorite schist in the Bergell tonalite aureole (Italy). American Journal of Science, 272, 423-437.

Trommsdorff, V., and Evans, B.W. (1974) Alpine metamorphism of peridotite rocks. Schweizerische Mineralogische und Petrographische Mitteilungen, 54, 333-352.

Trommsdorff, V., and Evans, B.W. (1980) Titanian Hydroxyl-Clinohumite: Formation and Breakdown in Antigorite Rocks (Malenco, Italy). Contributions to Mineralogy and Petrology, 72, 229-242.

Trommsdorff, V. (1983) Metamorphose magnesiumreicher Gesteine: Kritischer Vergleich von Natur, Experiment und thermodynamischer Datenbasis. Fortschr Mineral, 61, 283-308,

Trommsdorff, V., López Sánchez-Vizcaíno, V., Gómez-Pugnaire, M.T., and Müntener, O. (1998) High pressure breakdown of antigorite to spinifex-textured olivine and orthopyroxene, SE Spain. Contributions to Mineralogy and Petrology, 132, 139-148.

Uehara, S., and Kamata, K. (1994) Antigorite with a large supercell from Saganoseki, Oita Prefecture, Japan. The Canadian Mineralogist, 32, 93-103.

Uehara, S. (1998) TEM and XRD studies of antigorite superstructure. The Canadian Mineralogist, 36, 1595-1605.

Uehara, S. and Shirozu, H. (1985) Variations in chemical composition and structural properties of antigorites. Mineralogical Journal, 12, 299-318.

Ulmer, P., and Trommsdorff, V. (1995) Serpentine Stability to Mantle Depths and Subduction- Related Magmatism. Science, 268, 858-861.

Ulmer, P., and Trommsdorff, V. (1999) Phase relations of hydrous mantle subducting to 300 km. Mantle Petrology, 259-281.

Viti, C., and Mellini, M. (1996) Vein antigorites from Elba Island, Italy. European Journal of Mineralogy, 8, 423-434.

Wassmann, S., Stöckhert, B., and Trepmann, C.A. (2011) Dissolution precipitation creep versus crystalline plasticity in high-pressure metamorphic serpentinites. Geological Society, London, Special Publications, 360(1), 129-149.

Whitney, D.L., and Evans, B.W. (2010) Abbreviations for names of rock-forming minerals. American Mineralogist, 95, 185-187.

Whittaker, E.J.W. (1953) The structure of chrysotile. Acta Crystallographica, 6, 747-748.

Whittaker, E.J.W. (1956) The structure of chrysotile. II. Clino-chrysotile. Acta Crystallographica, 9, 855-862.

Worden, R.H., Droop, G.T.R., and Champness, E. (1991) The reaction antigorite↔olivine + talc + H_2O in the Bergell aureole, N. Italy. Mineralogical Magazine, 55, 367-377.

Wunder, B., and Schreyer, W. (1997) Antigorite: High-pressure stability in the system MgO-SiO_2-H_2O (MSH). Lithos, 41, 213-227.

Wunder, B. (1998) Equilibrium experiments in the system MgO-SiO_2-H_2O (MSH): stability fields of clinohumite-OH [$Mg_9Si_4O_{16}(OH)_2$], chondrodite-OH [$Mg_5Si_2O_8(OH)_2$] and phase A ($Mg_7Si_2O_8(OH)_6$). Contributions to Mineralogy and Petrology, 132, 111-120.

Wunder, B., Wirth, R., and Gottschalk, M. (2001) Antigorite: Pressure and temperature dependence of polysomatism and water content. European Journal of Mineralogy, 13, 485-495.

This is a preprint, the final version is subject to change, of the American Mineralogist (MSA)
Cite as Authors (Year) Title. American Mineralogist, in press.
DOI: https://doi.org/10.2138/am-2020-7159

FIGURE CAPTIONS

FIGURE 1. Stability field of serpentines (revised after Ghaderi et al. 2015). Purple solid curve: theoretical phase boundary between Liz and Atg+Brc assemblage determined by Ghaderi et al. (2015); Purple dashed curve: theoretical phase boundary rescaled to the experimental transition temperature at ambient pressure, while keeping the same functional form (Ghaderi et al. 2015); Blue area: geotherms of cold subduction zones (D80 models in Syracuse et al. 2010); Orange area: Liz/Atg phase boundary determined by Evans (2004); Yellow area: Liz/Atg phase boundary inferred from petrological observations (Schwartz et al. 2013); Yellow solid curve represents the partially dehydration of antigorite: Atg+Brc=Ol+Chl+H_2O (Shen et al. 2015); (i), (ii), (iii), (iv), (v)，(vi) and (vii) represent the complete decomposition of antigorite to form Ol+Opx±Chl+H_2O (at high pressure) or Ol+Tlc±Chl+H_2O (at low pressure) determined by different researchers, respectively: (i) red solid curve (Ulmer and Trommsdorff 1995); (ii) dark green solid curve (Wunder and Schreyer 1997); (iii) light green solid curve (Bose and Navrotsky 1998); (iv) orange solid curve (Bromiley and Pawley 2003); (v) blue solid curve (Hilairet et al. 2006; Nestola et al. 2010); (vi) black solid curve (Shen et al. 2015); (vii) indigo blue solid curve (Padrón-Navarta et al. 2010); Dashed pink curve shows the dehydration of antigorite under water absent conditions (Perrillat et al. 2005); Dashed orange lines indicate the high pressure transformation of antigorite (Bezacier et al. 2013).

FIGURE 2. BSE images of the HP experimental run products showing mineral assemblages of each runs (a, c, e, g, i) and antigorites selected for FIB preparation and TEM investigation (b, d, f, h, j).

FIGURE 3. Raman spectra in the range of 100-1100 cm^{-1} for antigorites in Fig. 2b, 2d, 2f, 2h, 2j respectively, and the P-T conditions of each run are presented in the

893 figures.

894

895 **FIGURE 4.** TEM images of antigorite in different runs. (a-b) HRTEM images of
896 antigorite in run D1512 and C4408, showing *a* cell parameter (*m* value) changing
897 even in a single grain. (c) Low magnification TEM image of antigorite growing
898 together with chlorite. Antigorite shows a changing *a* cell parameter and chlorite
899 has a *c* cell parameter *d*=14.07 Å. (d) HRTEM image of antigorite from run
900 D1526 showing stacking disorder along the *a*-axis.

901

902 **FIGURE 5.** HRTEM images of antigorite and chlorite (a-c), and antigorite and TiCl
903 reaction boundaries (d). (a) Antigorite reacted to chlorite in run D1512, and near
904 the reaction boundary, the *m* value of antigorite changes from 18 to 16. (b)
905 Antigorite and chlorite have an irregular reaction boundary in run C4408. (c)
906 Antigorite gradually decomposes to form chlorite and near the boundary the *m*
907 value of antigorite decreases. (d) Antigorite intergrown with Ti-clinohumite in
908 run D1526. In the white box the lattice fringes of antigorite are gradually
909 replaced by lattice fringes of Ti-clinohumite.

910

911 **FIGURE 6.** Distribution of periodicities in terms of *m* values in antigorite from
912 different runs. Run number and experimental conditions are given at the top of
913 each panel (a-e). (f) The distribution of the average *a*-axis *d*-spacing in different
914 runs with the average *m* values shown on the top.

915

916 **FIGURE 7.** P, T-dependence of peak *m* value of antigorite determined by
917 experimental results. The dark green line represents Ti-chondrodite-in line and
918 the dark red curve represents the antigorite dehydration reaction as determined
919 by Shen et al. (2015). The runs are plotted in the diagram and the peak *m* values
920 measured are listed. The dark yellow to light yellow colours represent the
921 decrease of antigorite in the run products. The bold italic numbers separated by
922 black lines represent the *m*-isoline distribution in P-T diagram.

FIGURE 8. Distribution of periodicities in terms of *m* values in sample C11107 from Tianshan antigorite (China). (a) Distribution using the "powder" preparation technique. (b) FIB sample of low-Al antigorite with Al_2O_3=1.11 wt.% (3.1D). (c) FIB sample of high-Al antigorite with Al_2O_3=3.38 wt.% (4.2H).

FIGURE 9. HRTEM images of natural antigorite from Tianshan, China (a-d). In sample 3.1D and 4.2H, the *m* values change even in a single grain, with microstructural disorder shown. The antigorite has a *c* cell parameter d=6.97 Å (b) and d=7.04 Å (c). Chlorite intergrowths in antigorite have a *c* cell parameter d=14.28 Å (d). (e) Antigorite and chlorite grain boundary in sample 4.4H, with *c* cell parameter of antigorite d=6.95 Å and *c* cell parameter of chlorite d=14.67 Å. (f) Chlorite intergrowths with antigorite in 4.4H, with *c* cell parameter of antigorite d=7.14 Å and *c* cell parameter of chlorite d=13.94 Å.

FIGURE 10. P-T-*m*-value diagram for antigorite determined by our experimental results and data in the literature (modified after Wunder et al. 2001). Red dotted lines display *m*-isolines (labelled by red italic numbers) of synthetic antigorite in the MSH system determined by Wunder et al. (2001). (M): *m*=17 natural antigorite from Malenco (Mellini et al. 1987). (A): *m*=14-15 in natural antigorite from Cerro del Almirez, Spain (Padrón-Navarta et al. 2008). (T-LAl): *m*=20-21 for low-Al antigorite and (T-HAl): *m*=19 for high-Al antigorite in natural antigorite from Tianshan, China (Shen et al. 2016 and this study). (C): *m*=15-16 in natural antigorite from Central Cuba (Auzende et al. 2002). (MP-V): *m*=18-19 in natural antigorite from Monviso massif, western Alps, Italy (Auzende et al. 2006). [G] (Ghaderi et al. 2015), [E] (Evans et al. 1976) and [S] (Schwartz et al. 2013) represent the location of the lizardite to antigorite transformation. The chrysotile to antigorite transformation is taken from Evans et al. (1976) (pink solid line). Maximum stability fields of antigorite are shown as determined experimentally by Ulmer and Trommsdorff (1995) (U&T, 95), Wunder and

Schreyer (1997) (W&S, 97). The yellow-red circles represent the five runs in this study and the run numbers are listed. The black solid lines are the inferred *m*-isolines of antigorite in the P-T diagram (labelled by black numbers). The two light green dashed lines represent the geothermal condition of surface of the slab and the bottom of the slab (Syracuse et al. 2010).

FIGURE 11. Calculated water contents in antigorite as a function of *m* value at a fixed Al-content of 2.73 wt% Al_2O_3.

TABLE CAPTIONS

TABLE 1. Run conditions and run products in experiments.

TABLE 2. Antigorite compositions from the starting material (Al06-44) and different runs analyzed with SEM-EDS.

TABLE 3. EPMA data of antigorites performed TEM measurements in sample C11107, from southwestern Tianshan, China.

Fig1

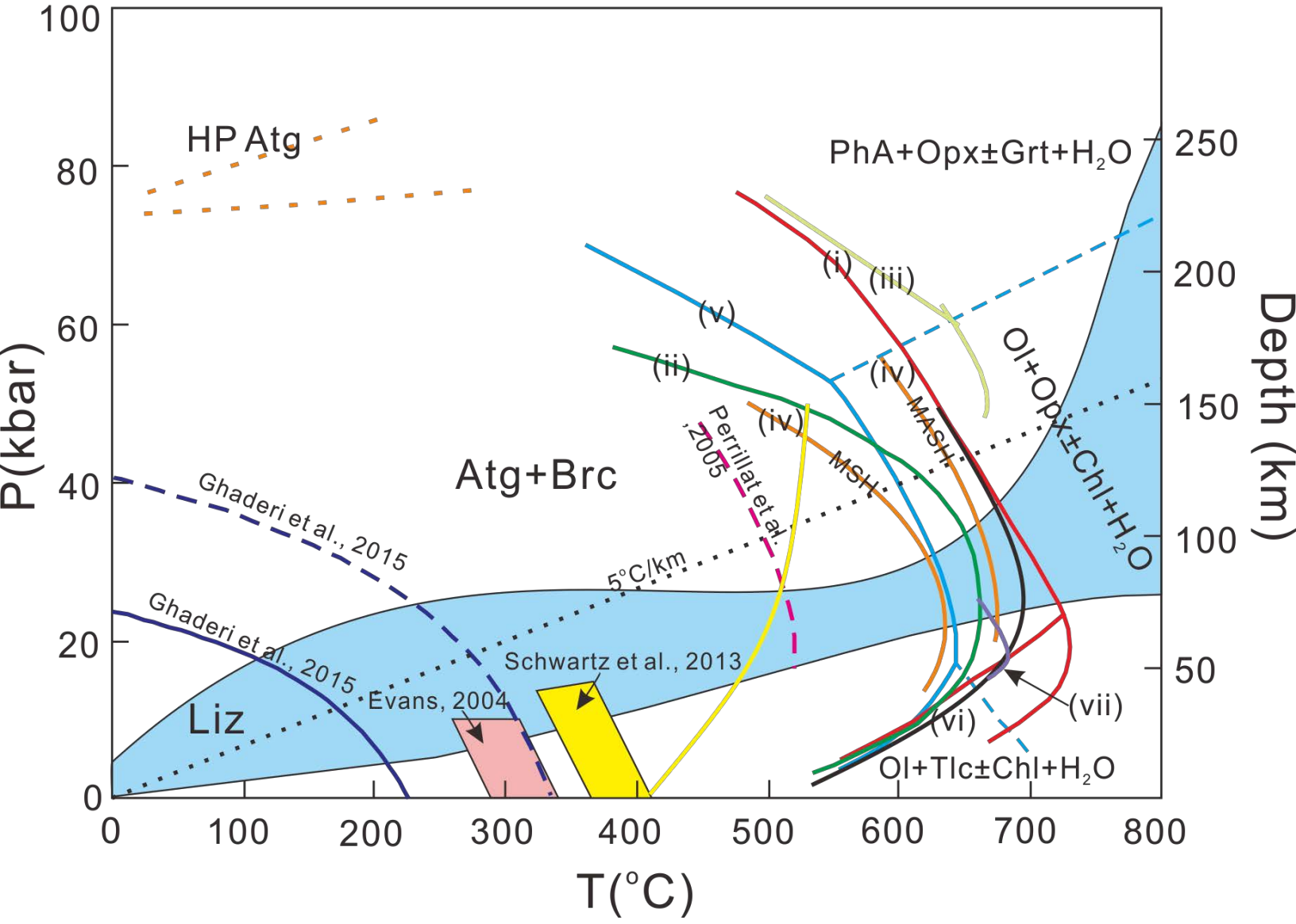
HP Atg
PhA+Opx±Grt+H2O
Ol+Opx±Chl+H2O
Ol+Tlc±Chl+H2O
Atg+Brc
Liz
(i)
(ii)
(iii)
(iv)
(v)
(vi)
(vii)
MASH
MSH
Perrillat et al., 2005
Ghaderi et al., 2015
Ghaderi et al., 2015
5°C/km
Schwartz et al., 2013
Evans, 2004
P(kbar)
Depth (km)
T(°C)
0
20
40
60
80
100
50
100
150
200
250
0
100
200
300
400
500
600
700
800

Fig 2-1

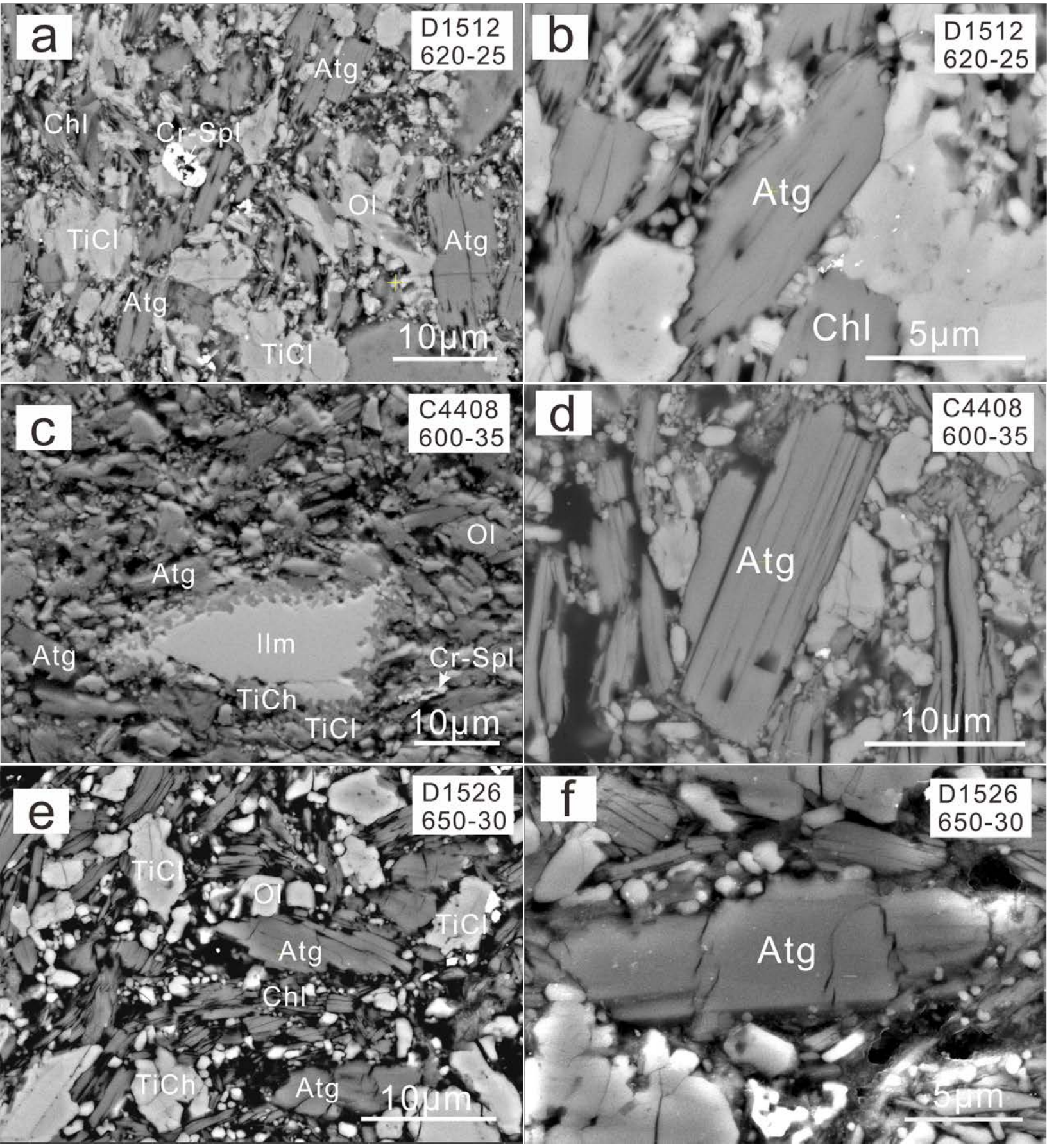
a
D1512
620-25
Atg
Chl
Cr-Spl
Ol
TiCl
Atg
Atg
TiCl
10μm
b
D1512
620-25
Atg
Chl
5μm
c
C4408
600-35
Ol
Atg
Ilm
Atg
Cr-Spl
TiCh
TiCl
10μm
d
C4408
600-35
Atg
10μm
e
D1526
650-30
TiCl
Ol
TiCl
Atg
Chl
TiCh
Atg
10μm
f
D1526
650-30
Atg
5μm

Fig 2-2

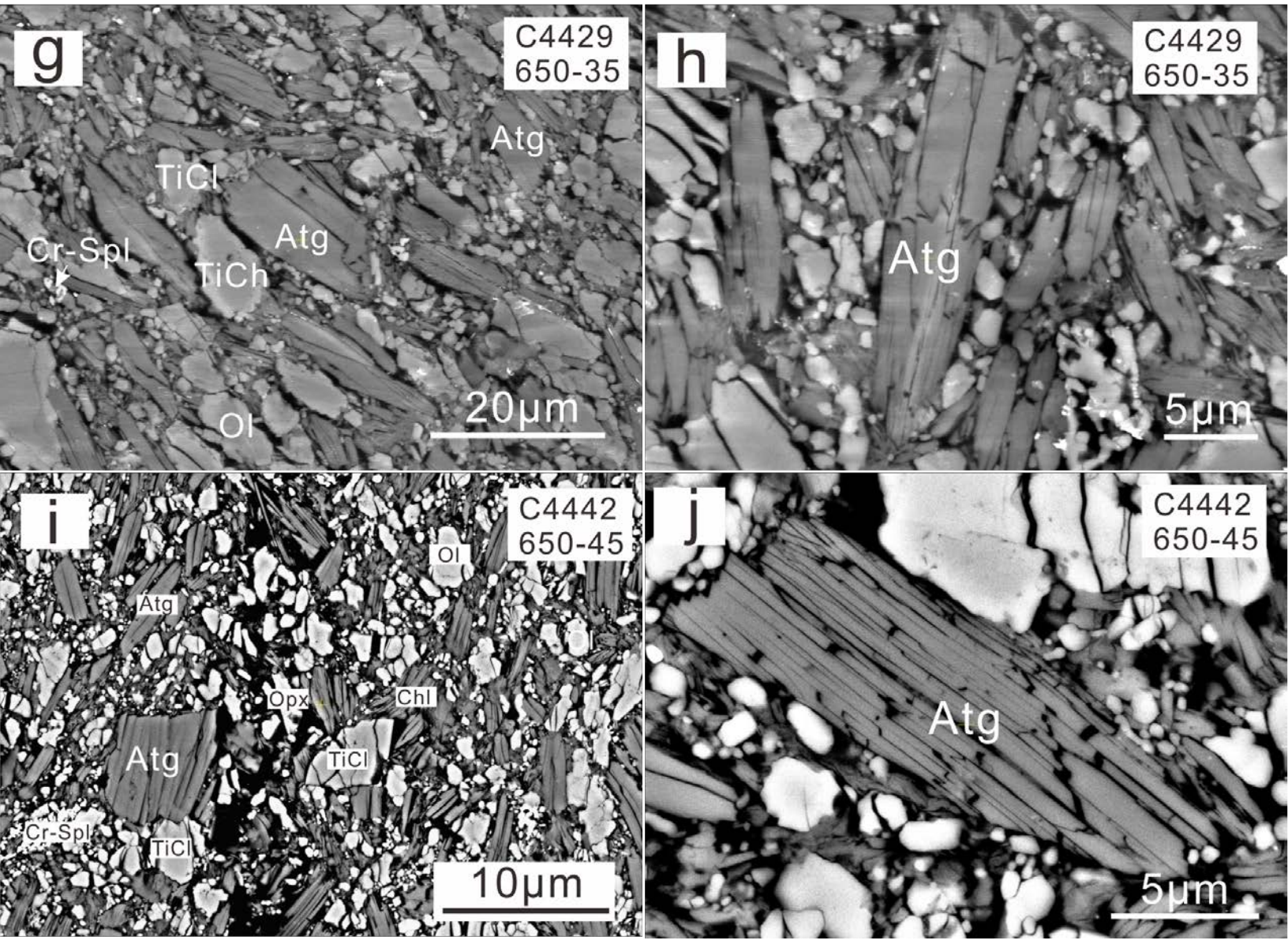
g
C4429
650-35
Atg
TiCl
Atg
Cr-Spl
TiCh
Ol
20μm
h
C4429
650-35
Atg
5μm
i
C4442
650-45
Ol
Atg
Opx
Chl
Atg
TiCl
Cr-Spl
TiCl
10μm
j
C4442
650-45
Atg
5μm

Fig 3

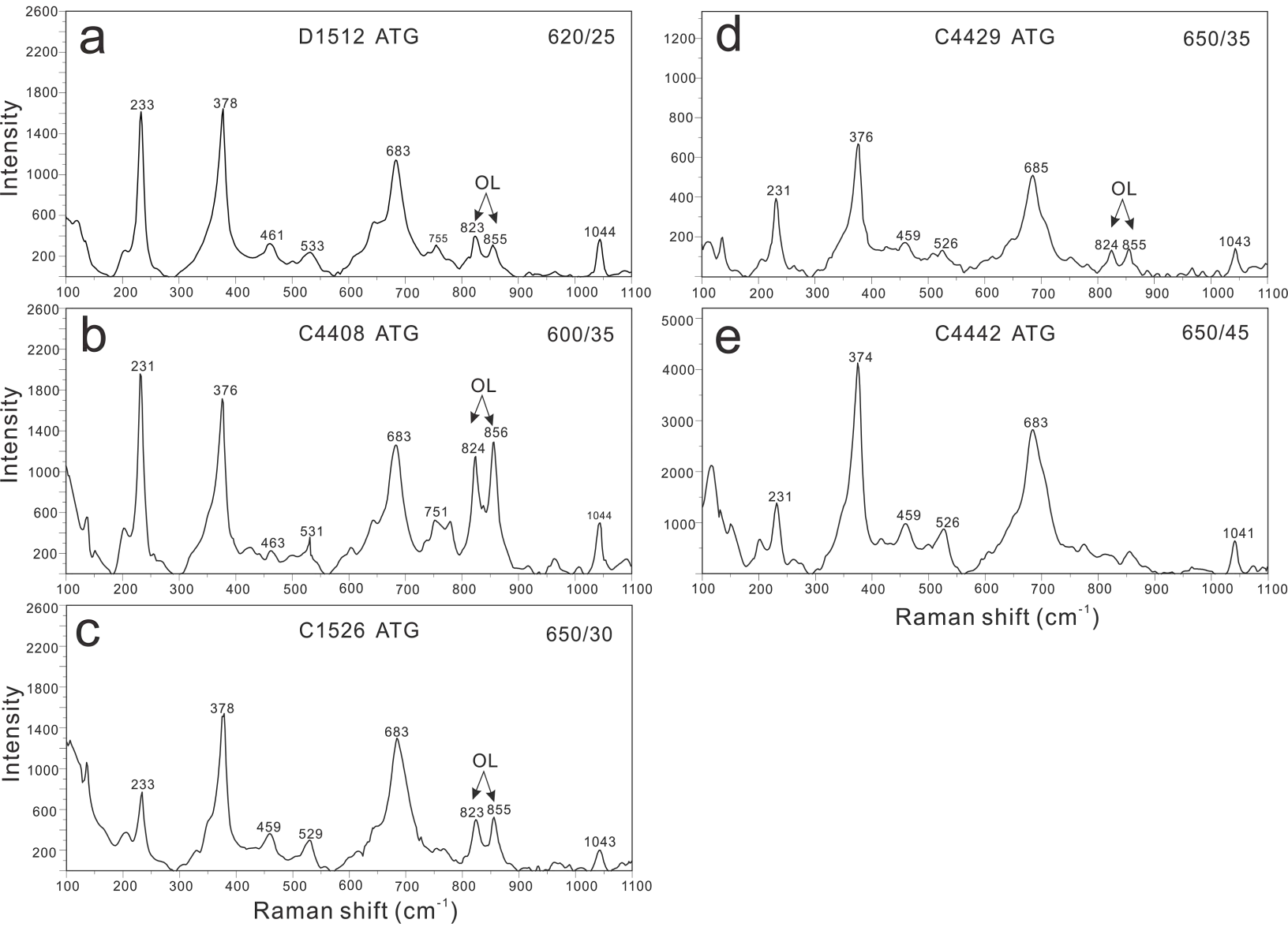
a
D1512 ATG
620/25
233
378
461
533
683
755
OL
823
855
1044
b
C4408 ATG
600/35
231
376
463
531
683
751
OL
824
856
1044
c
C1526 ATG
650/30
233
378
459
529
683
OL
823
855
1043
d
C4429 ATG
650/35
231
376
459
526
685
OL
824
855
1043
e
C4442 ATG
650/45
231
374
459
526
683
1041
Intensity
Raman shift (cm-1)

Fig 4

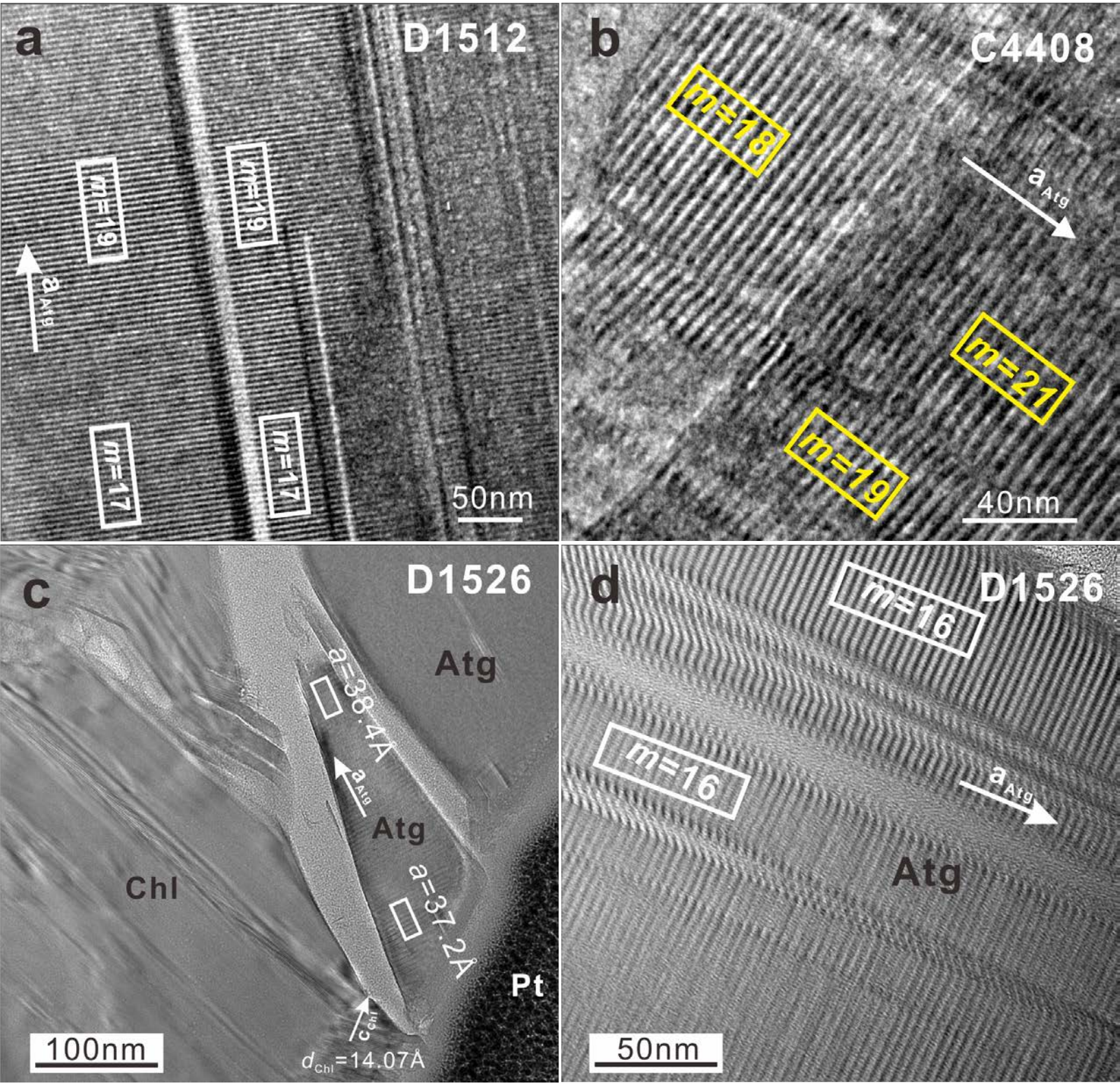
a
D1512
m=19
m=19
m=17
m=17
a Atg
50nm
b
C4408
m=18
a Atg
m=21
m=19
40nm
c
D1526
Atg
a=38.4Å
a Atg
Atg
Chl
a=37.2Å
Pt
c Chl
100nm
d Chl=14.07Å
d
D1526
m=16
m=16
a Atg
Atg
50nm

Fig 5

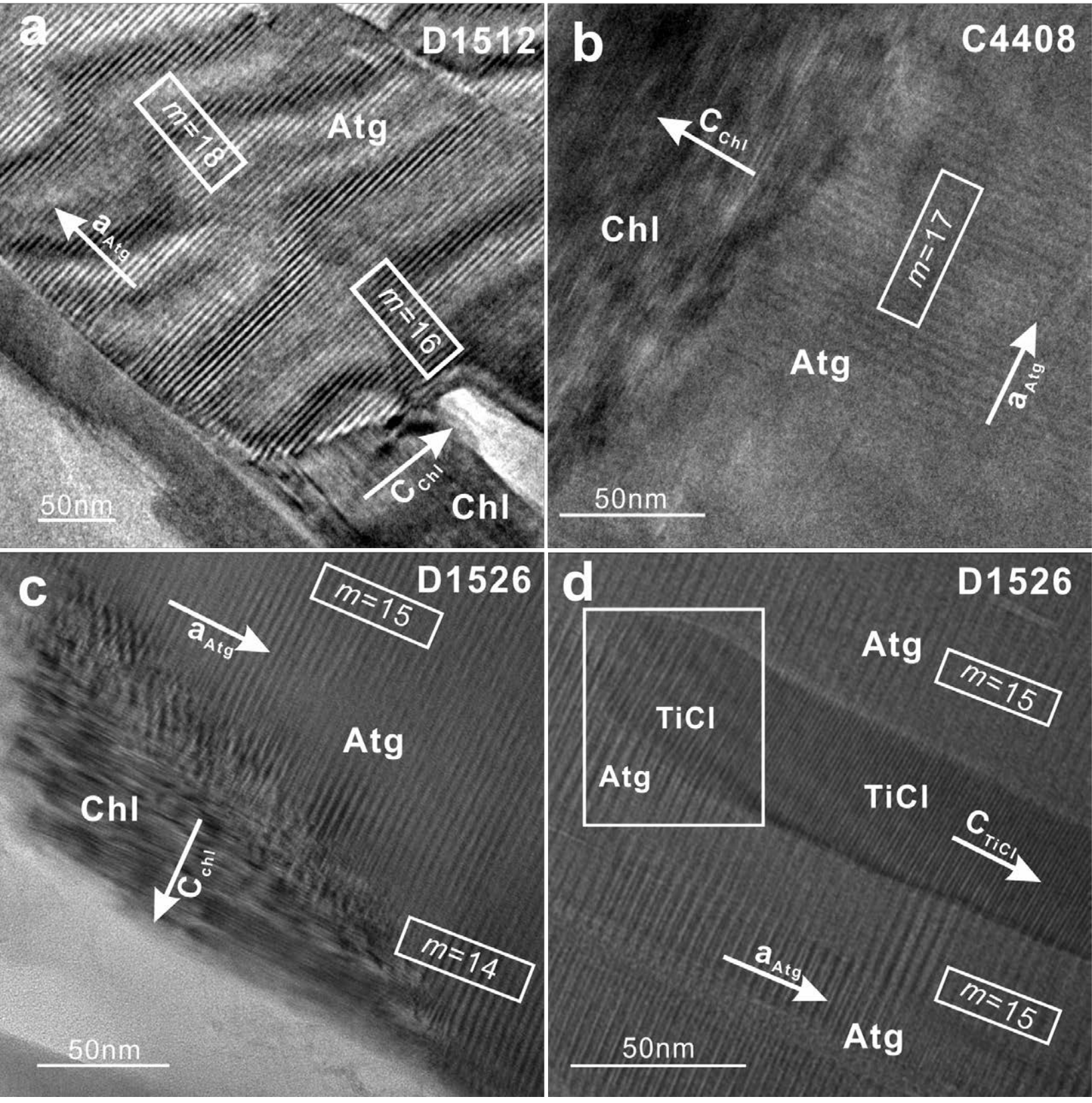
a
D1512
m=18
Atg
a Atg
m=16
C Chl
Chl
50nm
b
C4408
C Chl
Chl
m=17
Atg
a Atg
50nm
c
D1526
m=15
a Atg
Atg
Chl
C Chl
m=14
50nm
d
D1526
Atg
m=15
TiCl
Atg
TiCl
C TiCl
a Atg
m=15
Atg
50nm

Fig 6

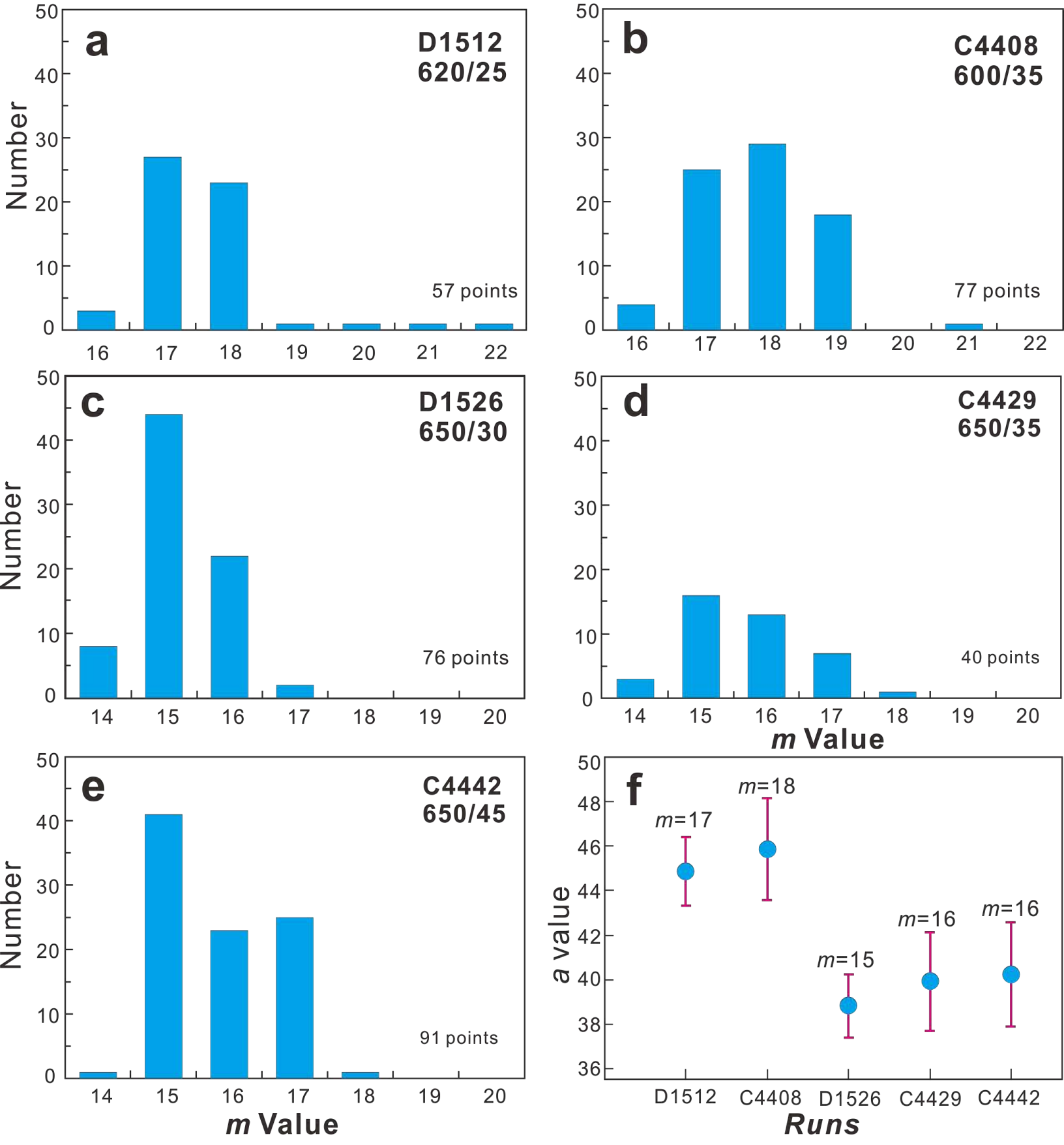
a
D1512
620/25
57 points
b
C4408
600/35
77 points
c
D1526
650/30
76 points
d
C4429
650/35
40 points
e
C4442
650/45
91 points
Number
m Value
f
m=17
m=18
m=15
m=16
m=16
a value
D1512
C4408
D1526
C4429
C4442
Runs

Fig 7

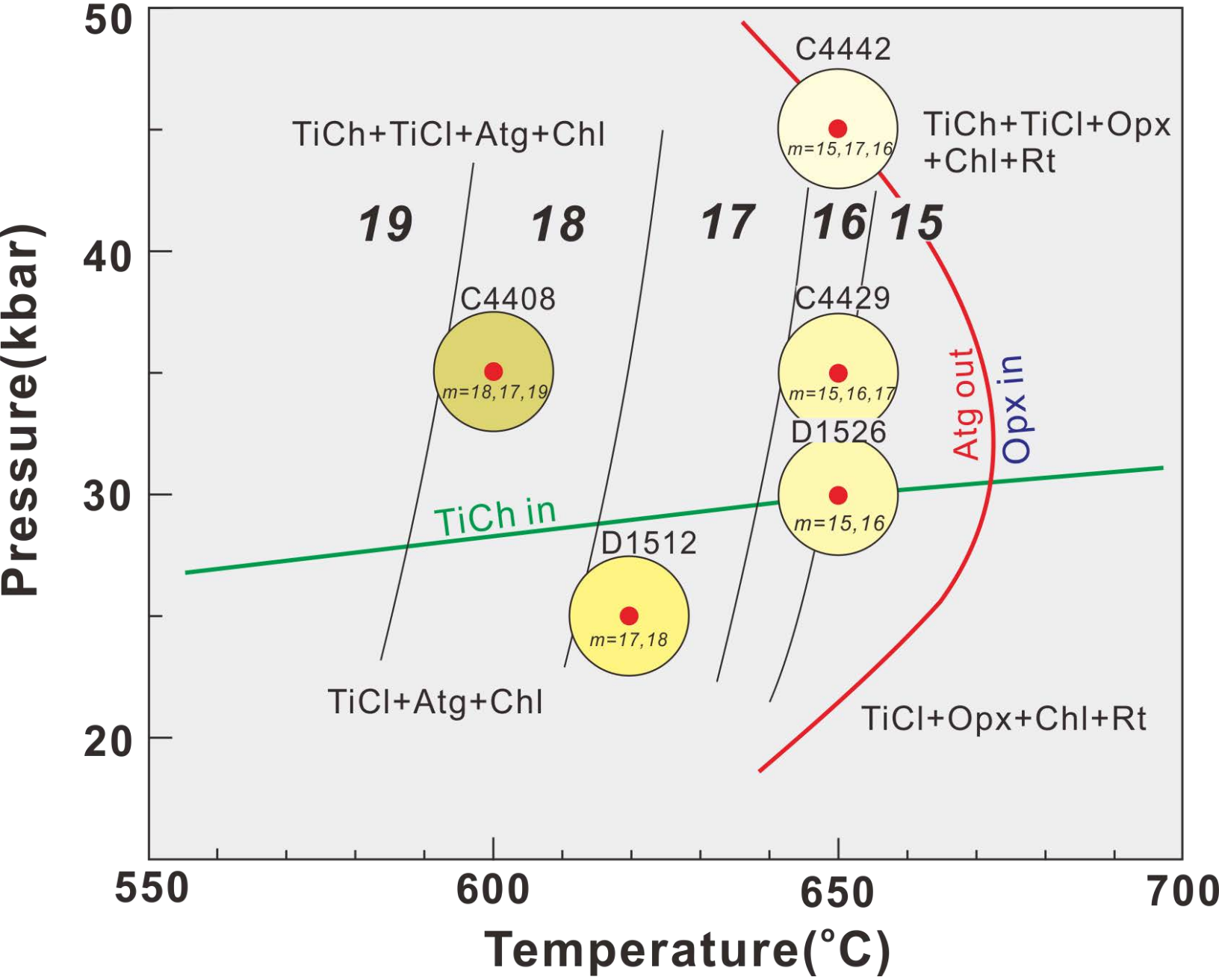
50
40
30
20
Pressure(kbar)
550
600
650
700
Temperature(°C)
C4442
m=15,17,16
TiCh+TiCl+Opx
+Chl+Rt
TiCh+TiCl+Atg+Chl
19
18
17
16
15
C4408
m=18,17,19
C4429
m=15,16,17
D1526
m=15,16
D1512
m=17,18
Atg out
Opx in
TiCh in
TiCl+Atg+Chl
TiCl+Opx+Chl+Rt

Fig 8

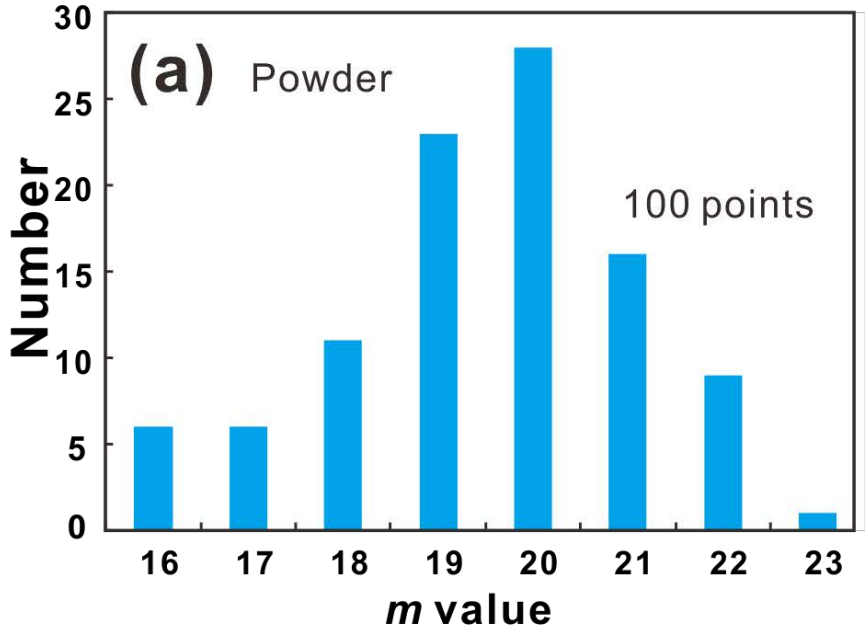
(a)
Powder
100 points
Number
m value
0
5
10
15
20
25
30
16
17
18
19
20
21
22
23

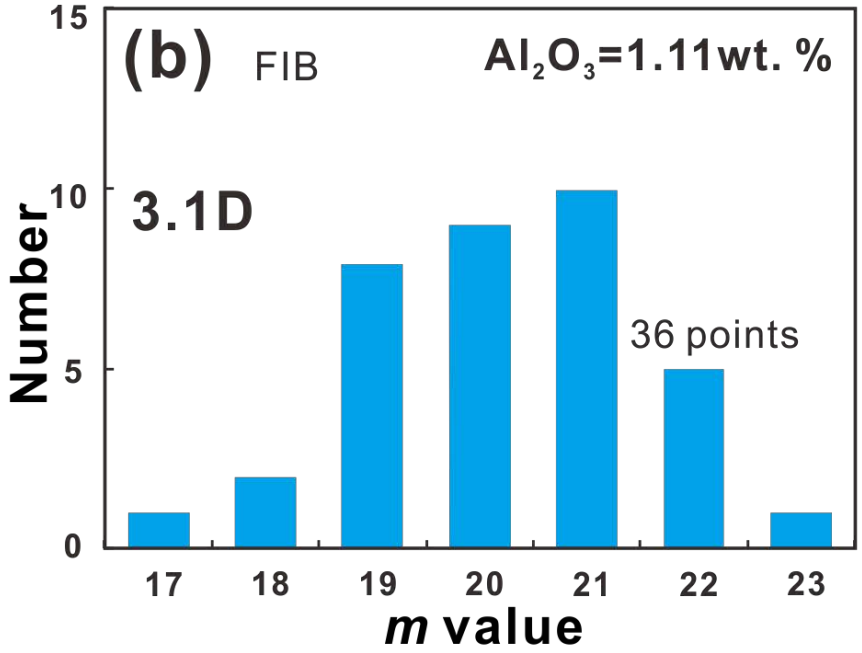
(b)
FIB
Al2O3=1.11wt. %
3.1D
36 points
Number
m value
0
5
10
15
17
18
19
20
21
22
23

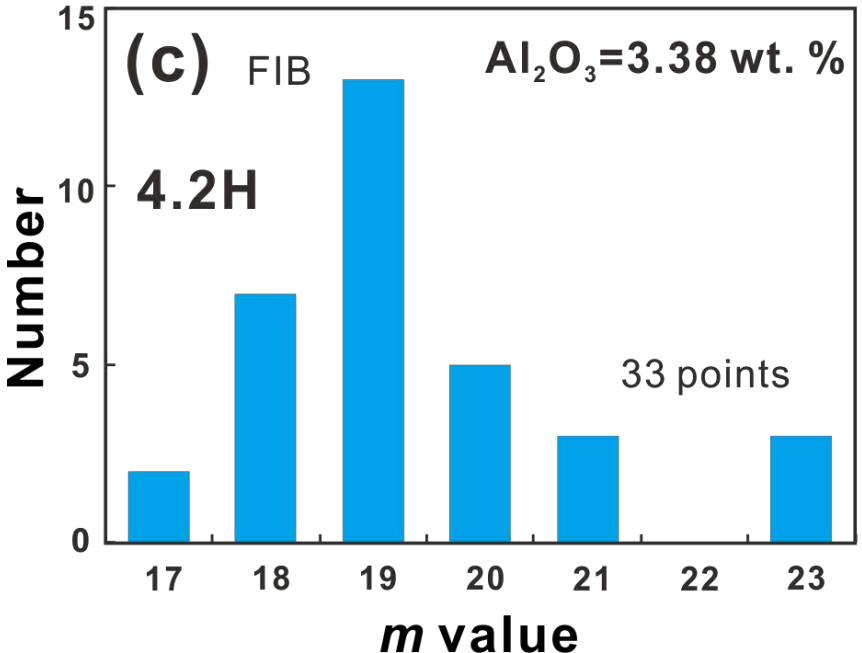
(c)
FIB
Al2O3=3.38 wt. %
4.2H
33 points
Number
m value
0
5
10
15
17
18
19
20
21
22
23

Fig 9

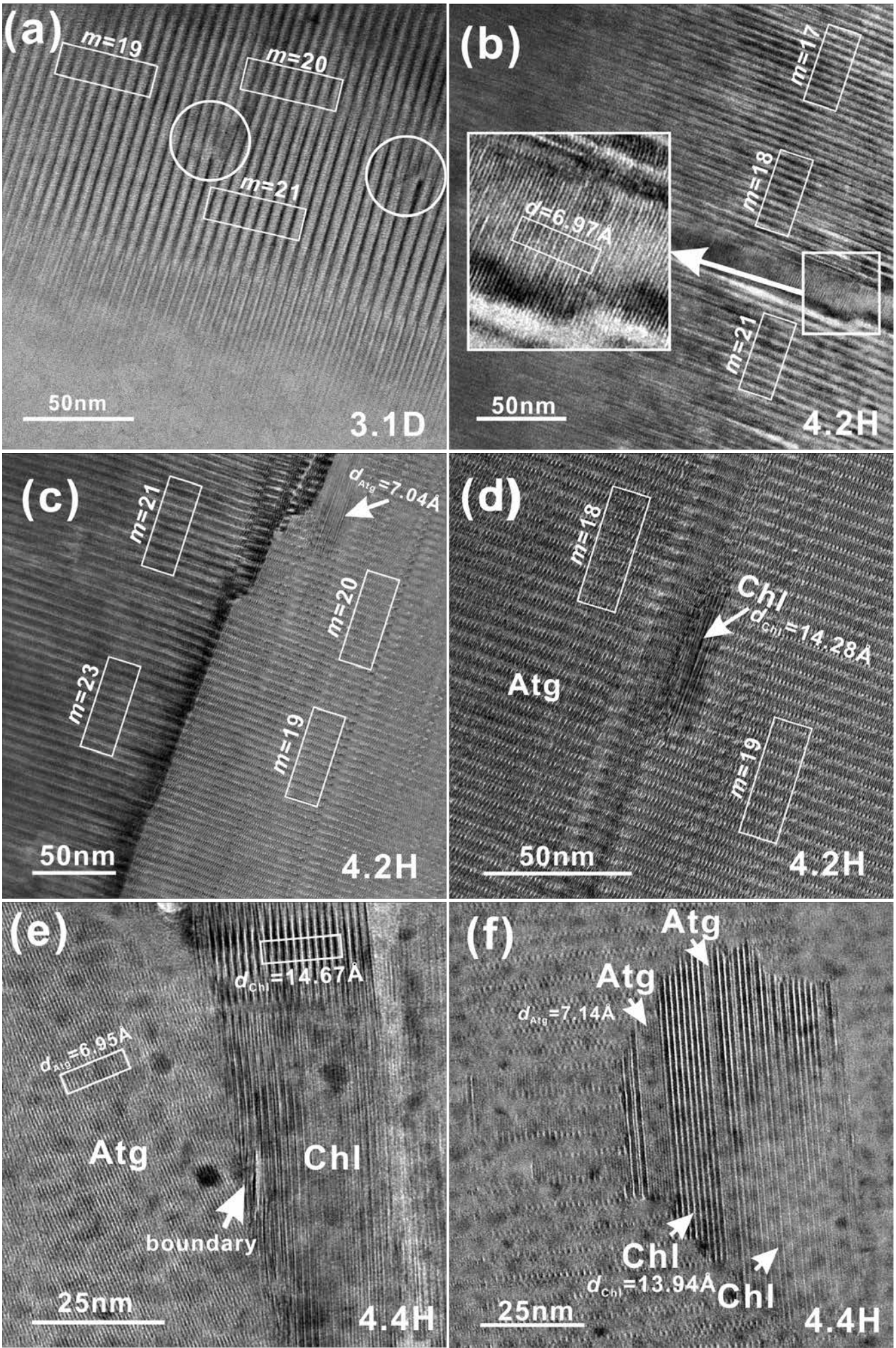
(a)
m=19
m=20
m=21
50nm
3.1D
(b)
m=17
m=18
d=6.97Å
m=21
50nm
4.2H
(c)
m=21
d_{Atg}=7.04Å
m=20
m=23
m=19
50nm
4.2H
(d)
m=18
Chl
d_{Chl}=14.28Å
Atg
m=19
50nm
4.2H
(e)
d_{Chl}=14.67Å
d_{Atg}=6.95Å
Atg
Chl
boundary
25nm
4.4H
(f)
Atg
Atg
d_{Atg}=7.14Å
Chl
d_{Chl}=13.94Å
Chl
25nm
4.4H

Fig 10

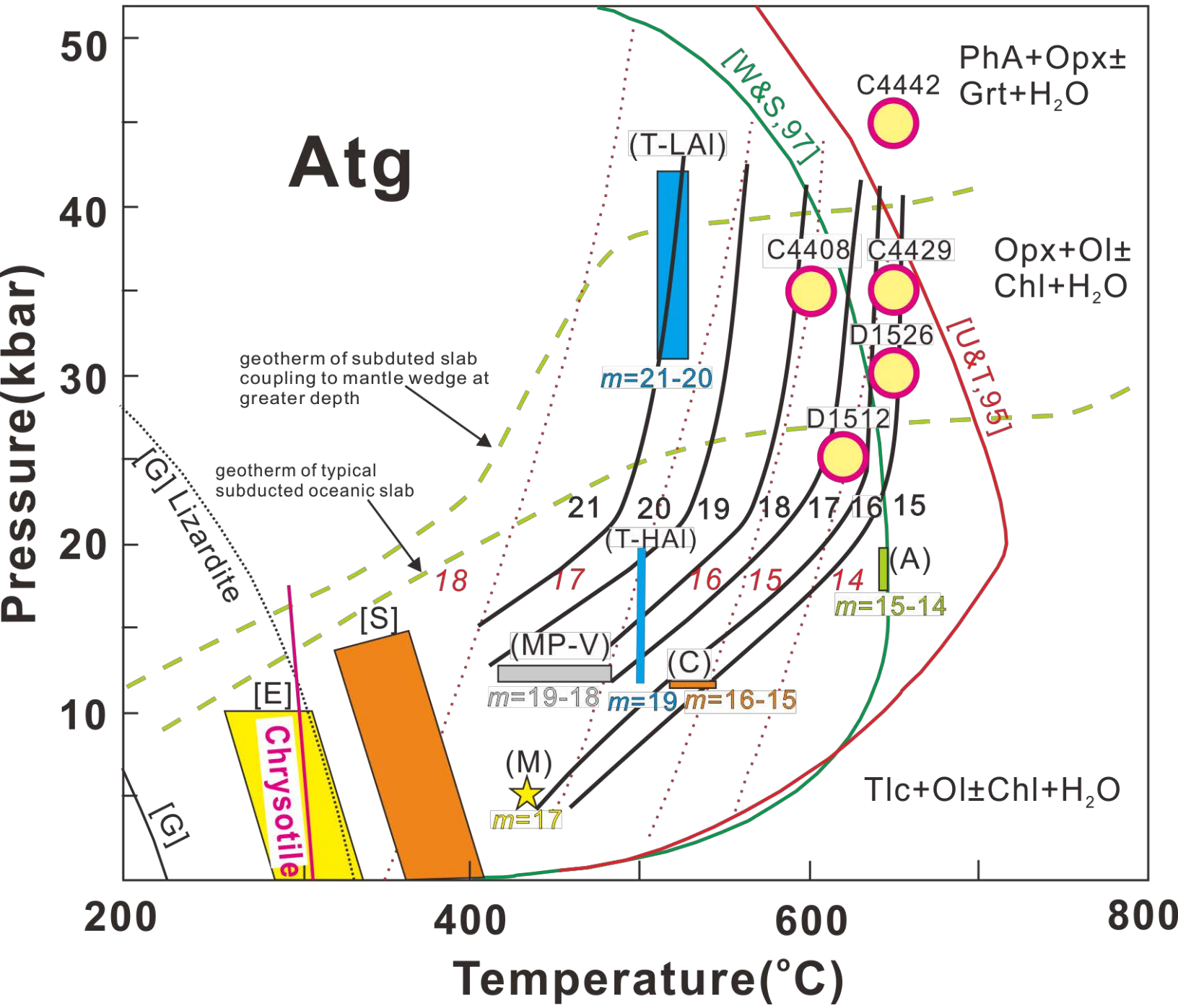
Atg
PhA+Opx±
Grt+H2O
Opx+Ol±
Chl+H2O
Tlc+Ol±Chl+H2O
C4442
C4408
C4429
D1526
D1512
[W&S,97]
[U&T,95]
(T-LAI)
m=21-20
(T-HAI)
(A)
m=15-14
(MP-V)
m=19-18
m=19
(C)
m=16-15
(M)
m=17
[S]
[E]
Chrysotile
[G] Lizardite
[G]
geotherm of subduted slab
coupling to mantle wedge at
greater depth
geotherm of typical
subducted oceanic slab
21
20
19
18
17
16
15
18
17
16
15
14
Pressure(kbar)
50
40
30
20
10
200
400
600
800
Temperature(°C)

Fig 11

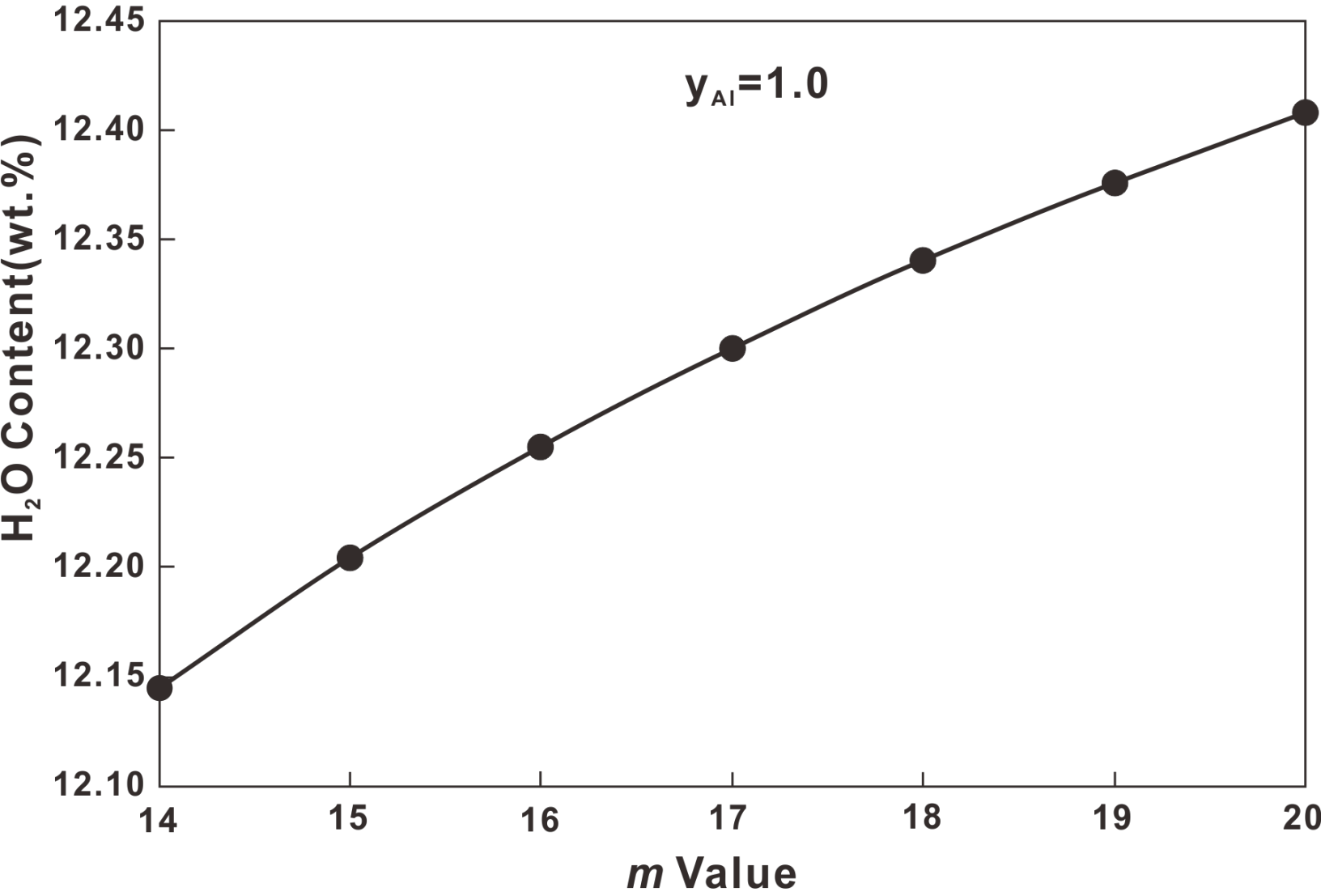
12.45
12.40
12.35
12.30
12.25
12.20
12.15
12.10
H2O Content(wt.%)
yAl=1.0
14
15
16
17
18
19
20
m Value

Table 1 Run conditions and run products in experiments.

Run No.	T (ºC)	P (kbar)	Hours	Run Products
D1512	620	25	168	Atg, TiCh, TiCl, Ol, Ilm, Cr-Spl, Chl(minor)
C4408	600	35	168	Atg, TiCh, TiCl, Ol, Ilm, Cr-Spl, Chl(minor)
D1526	650	30	168	Atg, TiCh, TiCl, Ol, Cr-Spl, Chl
C4429	650	35	168	Atg, TiCh, TiCl, Ol, Cr-Spl, Chl
C4442	650	45	168	Atg, TiCh, TiCl, Ol, Cr-Spl, Chl, Opx

Table 2 Antigorite compositions from the starting material (Al06-44) and different runs analyzed with SEM-EDS.

	Al06-44*		D1512		C4408		D1526		C4429		C4442	
	AVG(5)[#]	stdev	AVG(5)	stdev	AVG(5)	stdev	AVG(5)	stdev	AVG(5)	stdev	AVG(5)	stdev
SiO_2	42.46	0.19	41.58	0.87	40.91	0.96	41.32	0.61	41.95	0.45	41.55	0.25
Al_2O_3	2.65	0.16	2.78	0.18	2.67	0.28	3.23	0.26	2.87	0.16	3.00	0.20
Cr_2O_3	0.25	0.04	0.41	0.08	0.40	0.13	0.47	0.05	0.45	0.08	0.72	0.07
FeO	3.61	0.04	3.93	0.10	3.94	0.40	4.00	0.20	3.91	0.11	3.95	0.24
MgO	37.87	0.28	36.76	0.84	36.71	0.53	36.74	0.61	36.65	0.56	37.37	0.32
Total	85.11		85.46		84.76		85.76		85.83		86.59	
O	6.824		6.824	0.000	6.824	0.000	6.824	0.000	6.824	0.000	6.824	0.000
Si	1.928		1.931	0.021	1.920	0.036	1.918	0.011	1.941	0.011	1.904	0.011
Al	0.142		0.152	0.009	0.147	0.015	0.177	0.014	0.156	0.008	0.162	0.011
Cr	0.009		0.015	0.003	0.015	0.005	0.017	0.002	0.016	0.003	0.026	0.002
Fe	0.137		0.153	0.006	0.155	0.017	0.155	0.007	0.151	0.004	0.151	0.010
Mg	2.563		2.545	0.025	2.568	0.046	2.542	0.012	2.528	0.010	2.554	0.022
sum	4.779		4.812	0.013	4.805	0.026	4.809	0.005	4.792	0.007	4.798	0.012

[*] The composition data of Al06-44 was cited from Debret et al. 2015. All the structual formulae were calculated based on antigorite polysome *m*=17.

[#] AVG(5) means the average of 5 points analyses.

Table 3 EPMA data of antigorites performed TEM measurements in sample C11107, from southwestern Tianshan, China.

Comment	**3.1D**	**4.2H**	**4.4H**
SiO_2	44.16	41.96	42.47
TiO_2	0.05	0.04	0.00
Al_2O_3	1.11	3.38	2.43
Cr_2O_3	0.18	0.39	0.60
FeO	2.56	2.73	2.84
MnO	0.02	0.03	0.00
MgO	38.95	38.23	38.75
NiO	0.11	0.07	0.18
Total	87.14	86.83	87.27
O	6.824	6.824	6.824
Si	1.997	1.911	1.929
Ti	0.002	0.001	0.000
Al	0.059	0.181	0.130
Cr	0.006	0.014	0.022
Fe	0.097	0.104	0.108
Mn	0.001	0.001	0.000
Mg	2.625	2.596	2.623
Ni	0.004	0.003	0.007
sum	4.791	4.812	4.818
X_{Mg}*	0.964	0.961	0.961

* X_{Mg}=Mg/(Mg+Fe)